HALEY E. BELL ALEXANDER

Candidate

ELECTRICAL ENGINEERING

Department

This dissertation is approved, and it is acceptable in quality and form for publication on microfilm:

Approved by the Dissertation Committee:

_____, Chairperson

_____

_____

_____

_____

_____

_____

Accepted:

_____

Dean, Graduate School

_____

Date

DATA-BASED CONTROL OF A MIMO SYSTEM IN THE PRESENCE OF UNCERTAINTY

BY

HALEY E. BELL ALEXANDER

B.S., Electrical Engineering, University of New Mexico, 2004

THESIS

Submitted in Partial Fulfillment of the
Requirements for the Degree of

Master of Science
Electrical Engineering

The University of New Mexico
Albuquerque, New Mexico

December, 2008

DEDICATION

To the Giants, whose accomplishments have paved the road toward my endeavors.

"*Pigmaei gigantum humeris impositi plusquam ipsi gigantes vident.*"

- Isaac Newton, 1676

Translation: If I have seen a little further it is by standing on the shoulders of Giants.

ACKNOWLEDGEMENTS

Funding for this effort was provided by the Air Force Research Laboratory. Dr. Seth L. Lacy of the Space Vehicles Directorate at Kirtland Air Force Base supervised the research described in this report. Dr. Karl N. Schrader, a Boeing Associate Technical Fellow at Boeing-SVS, Inc., served as program manager for this effort. Dr. Chaouki Abdallah, Professor and Chair of the Electrical and Computer Engineering department at the University of New Mexico, was my Academic Advisor. I wish to thank all of them for their mentorship and guidance, which was always constructive and greatly appreciated. I recognize Dale Parkes' contribution to this effort for his assistance in coding the algorithms that take the partial derivatives of modal canonical state-space matrices. I thank Dale Parkes and our co-worker, Kirk Lohnes, for their support and advice. I am indebted to my employer, Boeing-SVS, Inc., not only for their financial support of my pursuit of a Master's degree in Electrical Engineering, but also for their moral support. I appreciate the advice of Dr. Peter Dorato, Gardner-Zemke Professor Emeritus at the University of New Mexico, whose enthusiasm and mentorship inspired me to pursue a Master's degree in the first place. Special thanks goes to my husband, Michael Alexander, and our family and friends whose support and confidence in me were greatly appreciated.

DATA-BASED CONTROL OF A MIMO SYSTEM IN THE PRESENCE OF UNCERTAINTY

BY

HALEY E. BELL ALEXANDER

ABSTRACT OF THESIS

Submitted in Partial Fulfillment of the
Requirements for the Degree of

Master of Science
Electrical Engineering

The University of New Mexico
Albuquerque, New Mexico

December, 2008

DATA-BASED CONTROL OF A MIMO SYSTEM IN THE PRESENCE OF UNCERTAINTY

BY

HALEY E. BELL ALEXANDER
B.S., Electrical Engineering, University of New Mexico, 2004
M.S., Electrical Engineering, University of New Mexico, 2008

ABSTRACT

Temperature, radiation, vacuum, and other factors encountered in the space environment yield significant influence over the dynamic behavior of a payload system in orbit. Other factors affecting dynamic behavior may include the additional mass and damping characteristics of extensive cable harnesses, such as those required for actuated deployable systems. In extreme circumstances these factors can adversely affect stability of a control law derived from dynamic data collected on the ground or from flight data collected under unique environmental conditions. Although a robustly stable control law may be derived to accommodate varying environmental conditions, such robustness typically comes at the expense of the controller performance. In such circumstances, it may be possible to repeat the system identification process, assemble a new plant model and synthesize a control law from data collected on orbit. However, for systems of even moderate complexity this approach is time consuming, costly, and still may not yield the simultaneously desired stability robustness and performance margins.

This thesis explores a controller development approach that proposes the application of a cost metric for both stability and robustness based on directly measured frequency

response functions (FRF's) under operational conditions. These cost metrics are used to tune an existing control law such that the total cost is minimized, thereby precluding the need to perform additional system identification and modeling tasks on-orbit. The covariance of the measured FRF's are incorporated into the cost metric to ensure both robust stability and performance. Single-input, single-output (SISO) methods are extended to the multi-input, multi-output (MIMO) domain and gradient descent algorithms are modified accordingly with the guidance of previous work. The resulting tuning algorithm is verified using a simple Fast Steering Mirror (FSM) system with the intent to demonstrate viability before applying it to the more complex Deployable Optical Telescope system at the Air Force Research Laboratory Space Vehicles Directorate at Kirtland AFB.

TABLE OF CONTENTS

LIST OF FIGURES x

CHAPTER 1 INTRODUCTION 1

1.1 Background 1

1.2 Literature Review 5

1.3 Thesis Objectives and Overview 9

1.4 Summary 11

CHAPTER 2 METHODOLOGY 12

2.1 Algorithm Overview 12

2.2 Notation 12

2.3 Algorithm Details 14

2.3.1 System Architecture 14

2.3.2 Cost Functions 16

2.3.3 Parameterization 18

2.3.4 Gradient Descent 20

2.3.5 Tuning 26

2.3.6 Stability Determination 27

2.4 Summary 31

CHAPTER 3 CONTRIBUTIONS 32

3.1 Stability Cost Function 32

3.2 Stability Determination 34

3.3 Summary 36

CHAPTER 4 IMPLEMENTATION 37
4.1 Algorithm Flow Chart 37
4.2 System Overview 38
4.2.1 The DOT Structure 38
4.2.2 The FSM Structure 39
4.2.3 Order of Implementation 43
4.3 Results of Algorithm Application to the FSM Structure 44
4.3.1 FSM Cases Tested with the Tuning Algorithm 44
4.4 Results of Algorithm Application to the DOT Structure 56
4.4.1 DOT Cases Tested with the Tuning Algorithm 56
4.5 Summary 56
CHAPTER 5 CONCLUSIONS 57
APPENDIX A STABILITY ROBUSTNESS DERIVATIVE CALCULATION 60
REFERENCES 64

LIST OF FIGURES

Figure 1. Solid Model Rendering and Photo of Integrated DOT System 2

Figure 2. System Architecture in reference [1], General control system interconnection (left) and Standard feedback configuration (right) 14

Figure 3. System Architecture in reference [2] 15

Figure 4. FSM System Architecture 16

Figure 5. Quadrant Definition for CL Stability Determination 29

Figure 6. MIMO Nyquist Example 31

Figure 7. MIMO Nichols Example 31

Figure 8. Incorrect MIMO Nyquist Phase 35

Figure 9. Corrected MIMO Nyquist Phase 35

Figure 10. Flow chart of applied algorithm. 37

Figure 11. Current System Configuration 39

Figure 12. Suggested System Configuration 39

Figure 13. 3x2 MIMO Plant 40

Figure 14. FSM Dynamics 40

Figure 15. CL FSM System 41

Figure 16. Y Axis DSA Data Bode Plot 42

Figure 17. 3x2 Plant Using DSA Data 43

Figure 18. Subset of the Discrete State-Space *A* Matrix of the Actual FSM Compensator 45

Figure 19. Cost Function Progression for Stability Optimization 46

Figure 20. MIMO Nyquist Convergence for Stability Optimization 47

Figure 21. Zoom of MIMO Nyquist Convergence for Stability Optimization 47

Figure 22. Bode Plot for Stability Optimization 48

Figure 23. Zoom of Bode Plot for Stability Optimization 49

Figure 24. Cost Function Progression for Performance Optimization 50

Figure 25. MIMO Nyquist Convergence for Performance Optimization 50

Figure 26. Zoom of MIMO Nyquist Convergence for Performance Optimization 51

Figure 27. Bode Plot for Performance Optimization 51

Figure 28. Cost Function Progression for Weighted Performance Optimization 52

Figure 29. MIMO Nyquist Convergence for Weighted Performance Optimization..... 53

Figure 30. Zoom of MIMO Nyquist Convergence for Weighted Performance Optimization 53

Figure 31. Bode Plot for Weighted Performance Optimization 54

Figure 32. Cost Function Progression for Stability Optimization and Weighted Performance 55

CHAPTER 1 INTRODUCTION

This chapter provides a background of work done to date specifically on the Deployable Optical Telescope (DOT) and why that lead to the work documented in this thesis. The background is followed by a literature review to bring the reader up to date with the current knowledge on the topic; forming a basis for the goal of this thesis and justification for future research in this area. Finally, the objectives and overview are provided to clarify the focus of the thesis.

1.1 Background

Since the advent of space transportation systems, the concept of deployable large space structures (LSS's) has been on the minds of those in the scientific community. LSS's involve a high level of mechanical flexibility often combined with extremely accurate pointing and shape requirements. The same LSS characteristics defined in reference [12] still apply today:

- They are distributed parameter systems and therefore infinite dimensional in theory and very large dimensional in practice;
- They have many resonant low frequencies;
- Their natural damping is poorly known and very light;
- Prediction of their behavior in space via on-earth testing is limited;
- Requirements for shape, orientation, alignment, vibration suppression, and pointing accuracy are very stringent.

Based on the above characteristics, these structures tend to be actively controlled with a variety of sensors and actuators and that control is an extremely interdisciplinary subject

drawing on structural mechanics and dynamics, mathematical modeling and approximation of distributed parameter systems, optimization, estimation and control science, numerical analysis, and large-scale computation [12]. Control science has evolved greatly since the concept of LSS's was first considered and there have been many studies in the application of these advances to LSS controller design and implementation. Current knowledge on the subject can be found in the literature review of the following section, 1.2.

Figure 1. Solid Model Rendering and Photo of Integrated DOT System

The Deployable Optical Telescope (shown in Figure 1), is a large space structure. As explained in reference [13], it is a space traceable sparse-aperture telescope with deployable primary and secondary mirrors developed under the Large Deployable Optics program. This laboratory experiment has been and continues to be used to develop and evaluate technologies critical to the fielding of future large space telescopes.

As stated in reference [11], the deployable mirror segments must be precisely aligned relative to each other, and the optical pathways maintained to nanometer tolerances to

achieve the necessary optical wave-front coherence and image quality. The lightweight composite structure tends to exhibit lightly damped resonances that cause large-amplitude motion when excited. Low-frequency motion can induce pointing error and defocus and may be caused by gravity gradients, solar pressure, or thermal gradients. Higher-frequency motion can cause line-of-sight jitter and may be caused by small lurching in hinges or latches, popping or drying effects of composite materials, or excitation of structural modes by the spacecraft's attitude control system. Vibration above 100 Hertz poses the risk of coupling with optical elements, causing high-order wave-front distortions. Developing such a LSS therefore requires advances in many technical areas, including integrated system modeling and validation, active vibration control design and implementation, on-orbit system identification, structural and optical metrology, and wave-front sensing and control [11].

The control system developed for DOT was based on a variation of linear-quadratic-Gaussian (LQG) optimal setpoint control [6]. Low-bandwidth integrator-type control was used to maintain setpoint positions for each primary mirror segment. Upon each low-bandwidth controller, a wide-bandwidth dynamic output-feedback controller was implemented to provide active damping and wide-bandwidth ambient disturbance rejection. This full-order (344-state) LQG optimal output-feedback controller was developed based on MIMO system identification models. Since persistent disturbances, traceable to spacecraft subsystems associated with attitude control and thermal management, are not sufficiently attenuated with the broadband LQG controller, an

adaptive disturbance rejection controller can be applied as an outer loop around the LQG and setpoint controller.

Controller performance is contingent upon the quality of the system model used for controller synthesis. There are many options for system identification of a MIMO system. Those working on the DOT structure utilized a frequency-domain modeling approach which has many advantages: models can be identified in separate frequency bands and later combined to form a single model, frequency data need not be uniformly spaced, each data point in the frequency domain may be the result of significantly averaged time-domain data which reduces uncertainty and uncorrelated noise, and the excitation signals can be tailored to account for system properties such that signal-to-noise data in and around system zeros or poles can be optimized and sensor saturation avoided [11]. Data based models were created for the lightly damped, modally dense structure. Measured FRF information was captured and, along with it, corresponding variance information to quantify the uncertainty in data collection [13]. There are many sources of model uncertainty, too numerous to list here, that can enter into and corrupt a system model; thus affecting the performance of the controller synthesized from it. The model validation process used by those working on the DOT structure was extensive and time consuming. Even then, the inability to accurately simulate on-orbit conditions is a recognized model limitation. Also, time-varying system dynamics were observed. Based on these past findings, on-orbit system identification and controller tuning capability was identified as a necessary follow-on research effort for the development of a tactical space telescope design. That is what prompted the work presented in this thesis.

1.2 Literature Review

Prior work directly associated with or simply applicable to Large Space Structures, including deployable optical systems, is well documented in the open literature, but a few pertinent examples will be given here.

The development of large space structures has required advances in technical areas including integrated system modeling and validation, active vibration control design and implementation, on-orbit system identification, structural metrology and, in the case of optical space structures, optical metrology and wave-front sensing and control. Research in the 1970's and 1980's was typically performed at the component level but progressed to system-level hardware testing in the 1990's [11]. Reference [14] surveys the U.S. experimental facilities for control of flexible structures. A review of experimental test articles is available in the literature review of reference [1].

Work was done by Carrier and Aubrun [15] in the early 1990's on the Advanced Structures and Controls Integrated Experiment (ASCIE) at Lockheed Martin Advanced Technology Center. Their research focused on developing numerically tractable and robust methods to model and structurally control large, complex, flexible systems. Their research included evaluating how accurately the dynamic behavior of such a structure could be predicted using finite element analysis, developing structural control methods to improve segment alignment of a primary mirror and achieving wideband structural vibration suppression. Carrier and Aubrun used frequency-response functions measured with active control sensors and actuators to obtain modeling data because classical modal

testing of large systems is costly and difficult and using FRFs was more representative of on-orbit testing of space structures. They demonstrated methods to model system dynamics online, analytically determine modal characteristics offline, and synthesize system models for controller development from frequency-response measurements.

NASA has, of course, been at the forefront of LSS research and development through their own research centers as well as through contractors. Recent work by NASA includes its facilitation of the James Webb Space Telescope (JWST), which uses adaptive optics, wavefront sensing, and lightweight structures. See references [16-19] for more information. NASA has also supported many university studies [20].

The U.S. Air Force Research Laboratory (AFRL), Space Vehicles Directorate, has been involved in developing innovative solutions for the deployment and operation of LSSs. The AFRL established the Ultra-Lightweight Imaging Technologies Experiment (UltraLITE) program in 1995 to develop and demonstrate a variety of enabling technologies. Much of this program is documented in various papers, see references [21-23]. Several component-level flight experiments were accomplished as part of the UltraLITE program, including active vibration control and isolation experiments [24,25]. The DOT experiment, mentioned in the Background, section 1.1 above, was the final project completed under the UltraLITE program.

System identification for LSSs is typically performed in the frequency domain; recall the findings of Carrier and Aubrun. There are now several frequency domain system identification tools, such as DynaMod [26] which allows the modeler to add and remove

dynamics from the model, as well as tune the model using an iterative search algorithm based on several model fit metrics with frequency weighting. PAM-VA One [27] is a hybrid modeling tool that combines low-frequency deterministic modeling with statistical approximations for modally dense subsystems. More details on frequency domain system identification algorithms and methods can be found in references [11,13,26, 28-31].

After synthesis of an initial model, model tuning must commence in order to correct deficiencies and yield a model which is a more accurate match to measured data. Model synthesis algorithms tend to have difficulty fitting MIMO models with low-amplitude response at low frequency. A model can be improved in the low-frequency band by tuning with appropriate frequency-weighting matrices [11]. Correlation and error metrics can be used to improve efficiency and guide the model tuning process [32,33].

Disturbances must be considered depending on the LSS mission. Both the Hubble and James Webb deep space telescopes can afford to allow a long period of time for disturbances to dissipate on their own, whereas time-critical tactical missions necessitate the use of on-orbit system identification, active vibration isolation, and active vibration control to mitigate disturbances within the required timeline. The necessary bandwidth of the controller is largely determined by the on-orbit response and optometchanical coupling of the spacecraft. The need to balance passive structural stability and active control requirements for large optic systems is discussed in work by Lake et al. [34]. On-orbit system identification and controller tuning is recognized as a required capability because of the uncertainty surrounding the models used to create the controller. That

uncertainty includes mismodeling, where discrepancy exists between the physical reality of the system and the virtual model used for control design and performance prediction, design evolution, where the model is manipulated without necessarily improving it, and environmental factors, either unknown such as solar flux or insufficiently modeled, such as zero-gravity conditions [35]. A comprehensive list of spacecraft disturbances is presented in [36].

Many studies have been performed on sensor and actuator assessment, both open and closed-loop, for control effectiveness. A major component is actuator and sensor placement for the control problem. Reference [37] includes a literature review on the actuator placement problem for structural systems. References addressing closed-loop techniques include [38-40]. References addressing open-loop techniques, where the design model is analyzed without explicitly solving for the controller, include [1,41-49].

Controller synthesis involves designing a compensator for the open-loop system. Reference [50] is a classic reference on the synthesis of MIMO H_2 controllers. Reference [51] is more modern and includes H_∞ and μ synthesis controllers. Reference [52] compares several robust control synthesis techniques.

Controller tuning is a process to modify the closed-loop system by perturbing a baseline controller. Many control synthesis techniques can be applied as tuning techniques. Adaptive control and on-line tuning has a lack of spaceflight heritage and is less established. Some off-line controller tuning strategies include: $H_{2/\infty}$ design weight tuning

[51,53,54], Sensitivity-Weighted Linear Quadratic Gaussian tuning (SWLQG) [52, 55,56], Youla Parameter Tuning [57-62], Direct (Parameter Optimization) MIMO control [38,63-67]. The tuning methodology developed in reference [1] extends the direct (parameter optimization) tuning described in the previous references to capture robustness as an explicit element of the cost, to create a framework for a general controller parameterization, and to create capability to directly tune controllers with measured plant data; all limitations of the prior direct MIMO control techniques. That is why reference [1] was chosen as the foundation for the objectives of this thesis.

For more information on the topics mentioned above please see the literature review and body of reference [1].

1.3 Thesis Objectives and Overview

The performance and stability of a control law derived from a model-based synthesis approach is inherently dependent on the fidelity of the baseline model used in the synthesis process. Although models may be produced by a variety of techniques from finite-element analysis (FEA) to least-squares fit of measured time or frequency domain response functions, such models are typically representative of a limited set of environmental conditions present during the modeling process. Just as with most space systems, a dynamically controlled system may be assembled, modeled and tested in one environment, but subject to a vastly different ambient environment during actual operation.

In the operational environment a controller designed from a system identification model may become obsolete. System uncertainty arising from persistent disturbances, noise, un-modeled dynamics and nonlinearities may reduce the system performance or even prove unstable. Disturbances induced by the operational environment can include heat loading on a spacecraft as it enters and exits the earth eclipse. In the case of a multiple-input, multiple-output system where only measured frequency response and corresponding variance data is available, it may be useful to apply and extend an approach proposed in reference [1] that optimally tunes the baseline controller by minimizing a cost function that balances performance and robustness given measured system uncertainty. The use of variance data is a concept explored in reference [2]. Simulated validation is obtained from the application of this approach to a FSM system with the intent to obtain both simulated and experimental validation via application to the Deployable Optical Telescope (DOT) structure which resides at the Air Force Research Laboratory on Kirtland Air Force Base [3]. This approach may be applied to cases less extreme than the deployment of a space-based structure.

Areas recommended for future work in reference [1] which this thesis will address include:

- Exploration of the connection between the stability robustness metric and model uncertainty.
- The development and implementation of the tuning methodology in the discrete-domain as opposed to the continuous domain.

1.4 Summary

This chapter has explained the work leading up to this thesis, what its focus is, and why it is useful; thus preparing the reader for the following detailed description of the methodology used to achieve the objectives.

CHAPTER 2 METHODOLOGY

This chapter begins with an overview of the algorithm used in this thesis to generate an improved system compensator given a simulated baseline compensator and actual plant frequency response data with corresponding uncertainty data. It continues on to explain the details of the components of the applied algorithm and their dependency on system architecture.

2.1 Algorithm Overview

When a baseline controller is available and it is not convenient to re-characterize a system via complete system identification, tuning the baseline controller to accommodate changes in the dynamic behavior of the plant is an attractive option. As stated in reference [1], the tuning tool is based on forming an augmented cost function from weighting performance, stability robustness, deviation from the baseline controller, and controller gain. The tuning algorithm can operate with the plant's state-space design model or directly with the plant's measured frequency-response data. The controller is parameterized with a general tri-diagonal parameterization based on the real-modal state-space form. The augmented cost metric is chosen to be differentiable and a closed-loop, stability-preserving, nonlinear descent program is used to directly compute controller parameters that decrease the augmented cost. To automate the closed-loop stability determination in the measured-data-based designs, a rule-based algorithm is created to invoke the multivariable Nyquist stability criteria. This can be accomplished with only frequency response data.

2.2 Notation

$\Re$ – the field of real numbers

y – sensor measurement, $y \in \Re^{n_y}$

w – exogenous disturbances, including process and sensor noises, $w \in \Re^{n_w}$

x – plant state vector

u – actuator inputs, $u \in \Re^{n_u}$

ω – frequency vector (radians/second)

G – Plant FRF data over ω

K – compensator FRF data over ω

K_b – baseline compensator FRF data over ω

H – closed loop system

x_c – compensator state variable, $x_c \in \Re^{n_{x_c}}$

u_c – compensator input, $u_c \in \Re^{n_{u_c}}$

y_c – compensator input, $y_c \in \Re^{n_{y_c}}$

A_c, B_c, C_c, D_c – parameterized dynamic, input, output and feedthrough matrices of the State Space Compensator K of compatible dimensions: $A_c \in \Re^{n_{x_c} \times n_{x_c}}$, $B_c \in \Re^{n_{x_c} \times n_{u_c}}$, $C_c \in \Re^{n_{u_c} \times n_{x_c}}$, $D_c \in \Re$

p – compensator parameter vector

$K(p)$ – a specific parameter of the Compensator K

S_s – penalty term for deviations of max singular value of Sensitivity greater than threshold

S_{cr} – penalty term for distance of Nyquist locus to the critical point

$J(p)$ – cost function

α – cost function weighting scalar (between 0 and 1)

μ – stepsize

2.3 Algorithm Details

2.3.1 System Architecture

Three different system architectures were encountered during algorithm development. The architectures of reference [1], reference [2], and the FSM system are depicted in the figures below. All definitions are presented for MIMO systems unless otherwise noted. Each system architecture figure is followed by some corresponding equations. The nuances encountered vastly change the equations used and can lead to algorithm dysfunction if not implemented correctly.

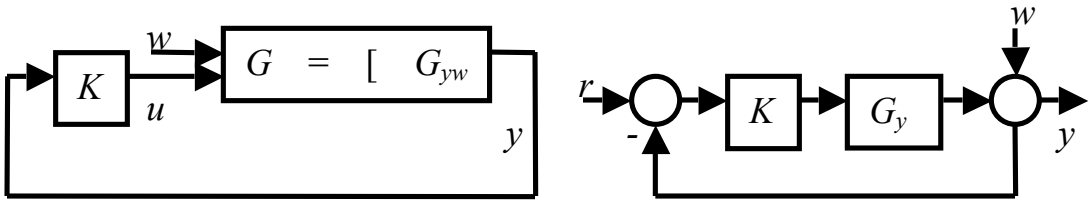

Figure 2. System Architecture in reference [1], General control system interconnection (left) and Standard feedback configuration (right)

The left diagram in figure 2 contains a plant, G, with a set of vector inputs and outputs: exogenous disturbances w, actuator inputs u, and sensor measurements y. A compensator, K, receives y as an input and generates actuator signals, u. Tracking is enabled, as shown in the right diagram of figure 2, by introducing a reference, r, at an appropriate location in the loop. With the compensator unconnected, one can obtain the open loop system. The systems feedback is defined in the compensator, K. When the compensator is appended to the dynamics of the open loop system one arrives at the closed loop system, H. The MIMO Sensitivity function, S, relates the exogenous disturbances, including

process noise, w to the output y. It defines the sensitivity of the closed loop response to perturbation in the open-loop.

$$u = Ky \tag{1}$$

$$y = G_{yw}w + G_{yu}u = G_{yw}w + G_{yu}Ky = [I - G_{yu}K]^{-1}G_{yw}w \tag{2}$$

$$u = K[I - G_{yu}K]^{-1}G_{yw}w \tag{3}$$

$$S = [I - G_{yu}K]^{-1} \tag{4}$$

$$H = K[I - G_{yu}K]^{-1}G_{yw} = KSG_{yw} \tag{5}$$

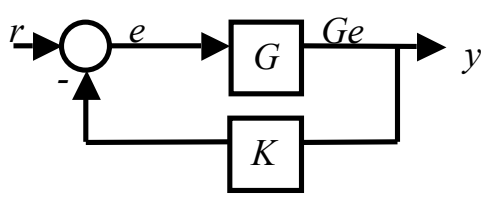

Figure 3. System Architecture in reference [2]

$$y = Ge \tag{6}$$

$$e = r - Ky = r - KGe = [I + KG]^{-1}r \tag{7}$$

$$y = G[I + KG]^{-1}r \tag{8}$$

$$S = [I + KG]^{-1} \tag{9}$$

$$H = G[I + KG]^{-1} = GS \tag{10}$$

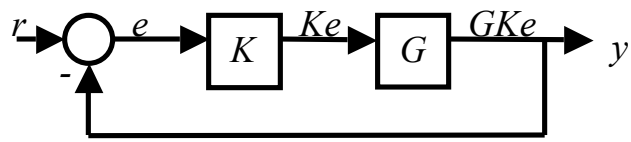

Figure 4. FSM System Architecture

The FSM architecture compensator receives the error signal as input.

$$y = GKe \tag{11}$$

$$e = r - y = r - GKe = [I + GK]^{-1} r \tag{12}$$

$$y = GK[I + GK]^{-1} r \tag{13}$$

$$S = [I + GK]^{-1} \tag{14}$$

$$H = GK[I + GK]^{-1} = GKS \tag{15}$$

It will be apparent in the formulations to follow how these architectures affect function definitions.

2.3.2 Cost Functions

The performance cost function is defined in reference [1] as an expression for the sensitivity of the performance as a function of the controller parameters, p. A regulator control problem is assumed. Since a white noise disturbance input is assumed (shown in Figure 2), the cost term is a summation of the closed loop (CL) cost over the frequency samples. H is a CL metric relating disturbance input to performance variables (the sensor suite y in this case). The cost function uses an H_2 root-mean-square (RMS) performance metric on the CL Transfer Function of the system to assess performance. This works

under the assumption that the system is stable so that the H_2 norm exists [6]. The H_2 norm is the RMS of the transfer functions impulse response, which measures the steady-state covariance of the output response, y, to unit white noise inputs, w. Smaller performance cost function magnitude indicates improved performance:

$$J_p(p) = \frac{1}{\pi}\sum_{k=1}^{n} trace\left(H_{cl}(j\omega_k)H_{cl}(j\omega_k)^H\right)\Delta\omega_k \tag{16}$$

H_{cl} is the closed loop system, defined above in equations (5), (10) or (15) depending on system architecture. And S is the sensitivity, defined above in equations (4), (9) or (14) depending on system architecture. $(\cdot)^H$ denotes the conjugate transpose.

The stability cost function, $J_s(p)$, is defined in reference [1] as a weighted combination of the Maximum Sensitivity Singular Value Stability Metric, S_s, and the Critical Point Distance Metric, S_{cr}:

$$J_s(p) = (1-\gamma_{cr})S_s(p) + \gamma_{cr}S_{cr}(p) \tag{17}$$

$$S_{cr}(p) = \frac{1}{\pi}\sum_{k=1}^{len(\omega)} W_{cr}(\omega_k)\frac{1}{d_{cr}^2(j\omega_k)}\Delta\omega_k \tag{18}$$

$$d_{cr}(j\omega) = \det(I + F(j\omega)) \tag{19}$$

S_s is the summation of the deviation of the maximum singular value of the sensitivity over a threshold in a frequency band of interest and S_{cr} is the summation of the inverse of the distance from the Multivariable Nyquist locus to the critical point over a frequency band of interest. For good stability robustness this distance is maximized near crossover.

γ_{cr} is a weighting term. In the interest of simplicity, the stability cost function was implemented with a weighting term of $\gamma_{cr} = 1$ so that the function uses the Multivariable Nyquist locus exclusively. Therefore, the equation for S_s will not be provided.
This yields a less conservative measure of stability robustness. The reasons for allowing this simplification of the stability cost metric are detailed in section 3.1.

$W_{cr}(\omega_k)$, from equation (18), is defined in reference [1] as a vector weighting function on the frequency values of interest, which also weights the relative contribution of the stability cost to the total cost. F, used in equation (19), is the systems loop transfer function (LTF) matrix and is dependent on system architecture. The term comes from the fact that $I+F = I-(-F)$, where $-F$ represents the transfer-matrix function around the loop in the presence of a subtraction block [6]. For reference [1], $-F = GK$ since the negative sign is defined as part of the compensator K. For reference [2], $-F=-KG$ since the negative sign is defined outside of the compensator K. For the FSM architecture, $-F=-GK$, since the negative sign is also defined outside of the compensator K.

There are weightings on the stability and performance cost functions that sum to create the total cost:

$$J(p) = \alpha J_p(p) + (1-\alpha) J_s(p) \tag{20}$$

2.3.3 Parameterization

For tuning, a full state-space parameterization of the compensator is desired. The baseline compensator FRF data is referred to as K_b and has the following state-space form (refer to the Notation in section 2.2 for dimensions, recall this is a MIMO system):

$$\dot{x}_c = A_c x_c + B_c u_c \tag{21}$$

$$u = y_c = C_c x_c + D_c u_c \tag{22}$$

State-space realizations are not unique so there are countless possible parameterizations. Reference [1] provides a study of some possible parameterizations, stating the Jordan canonical form as useful for understanding the form of the parameterization but having the flaws that not all systems can be diagonalized and some eigenvalues come in complex conjugate pairs so that each eigenvalue parameter is not independent, making the real/complex transition of the eigenvalues awkward. A near-modal state-space form is suggested where complex conjugate eigenvalues are grouped together and real eigenvalues are grouped in pairs, a second-order form is then applied. It is termed near-modal because of its resemblance to modal form with the inclusion of even pairs of real poles. Because the dynamics matrix is broken into 2x2 blocks corresponding to factors of the characteristic equation, a smoother transition from real to complex conjugate poles is obtained. Additionally, according to reference [1], most structural systems can be transformed into this form. However, multiple transformations and scaling are required to uniquely specify the matrices and improve numerical conditioning; which complicates the parameterization considerably.

When selecting a parameterization, it is important to consider that derivatives of the state-space representation of the compensator with respect to the parameters are required for all of the gradient computations. Derivatives of the near-modal form are relatively simple. The same is true of a modal parameterization, where the real eigenvalues appear

on the diagonal of the A_c matrix and the complex conjugate eigenvalues appear in 2x2 blocks on the diagonal of A_c. The modal transformation requires that the A matrix be diagonalizable. For example:

$$A_c = \begin{bmatrix} a_{11} & 0 & 0 & 0 \\ 0 & a_{22} & 0 & 0 \\ 0 & 0 & a_{33} & a_{34} \\ 0 & 0 & a_{43} & a_{44} \end{bmatrix} = \begin{bmatrix} a_1 & 0 & 0 & 0 \\ 0 & a_2 & 0 & 0 \\ 0 & 0 & a_3 & a_4 \\ 0 & 0 & -a_4 & a_3 \end{bmatrix} \tag{23}$$

$$B_c = \begin{bmatrix} b_{11} & b_{12} \\ b_{21} & b_{22} \\ b_{31} & b_{32} \\ b_{41} & b_{42} \end{bmatrix}, C_c = \begin{bmatrix} c_{11} & c_{12} & c_{13} & c_{14} \\ c_{21} & c_{22} & c_{23} & c_{24} \end{bmatrix}, D_c = \begin{bmatrix} d_{11} & d_{12} \\ d_{21} & d_{22} \end{bmatrix} \tag{24}$$

This parameterization was chosen for the FSM system in order to simplify the parameterization process. Cost function derivatives with such a parameterization are detailed in section 2.3.4.

Another parameterization suggestion in reference [1], referred to as Constrained Topology Parameterization, is something to keep in mind for systems where it is necessary to maintain integral action. As stated in reference [1], by fixing certain parameters in a free-topology controller parameterization, such as the near-modal parameterization, the controller topology can be constrained. Block diagonal controller topologies are generated by removing some controller parameters from the vector of tunable parameters, p.

2.3.4 Gradient Descent

Given the constant baseline compensator K_b, the tuned compensator is determined by the parameter vector, p. The gradients of the cost can be written as,

$$\nabla J(p) = \alpha \nabla J_p(p) + (1-\alpha)\nabla J_s(p) \tag{25}$$

where the gradient operator represents a vector formed of partial derivatives with respect to compensator parameters: $\nabla(\bullet) = \left[\frac{\partial(\bullet)}{\partial p_1} \cdots \frac{\partial(\bullet)}{\partial p_{n_p}}\right]^T$.

There is only one component of any of the applicable cost functions that contains the controller parameters and that is the compensator *K*. Thus, the gradient of any applicable cost function reduces to a multiplication of known matrices and the partial derivative of *K* with respect to controller parameters. Recalling the state space representation of *K*:

$$K = C_c(sI - A_c)^{-1} B_c + D_c \tag{26}$$

Its partial derivative with respect to controller parameters is:

$$\frac{\partial K}{\partial p_i} = \frac{\partial C_c}{\partial p_i}\phi_c B_c + C_c\phi_c \frac{\partial A_c}{\partial p_i}\phi_c B_c + C_c\phi_c \frac{\partial B_c}{\partial p_i} + \frac{\partial D_c}{\partial p_i} \tag{27}$$

The characteristic inverse is:

$$\phi_c = (Ij\omega - A_c)^{-1} \tag{28}$$

In the interest of processor efficiency, it is useful to look at the structure of the partial derivative of K as defined in equation (26) with respect to each parameter set and simplify the number of multiplications. Assuming the compensator is in modal canonical form, the A_c matrix contains complex pole pairs in 2x2 block form along its diagonal with the possibility of real poles on the diagonal and zeros elsewhere as exemplified in equation (23).

This results in the following possible structure of the characteristic inverse, ϕ_c:

$$\phi_c = \begin{bmatrix} j\omega - a_1 & 0 & 0 & 0 \\ 0 & j\omega - a_2 & 0 & 0 \\ 0 & 0 & j\omega - a_3 & -a_4 \\ 0 & 0 & a_4 & j\omega - a_3 \end{bmatrix}^{-1} = \begin{bmatrix} \frac{1}{j\omega - a_1} & 0 & 0 & 0 \\ 0 & \frac{1}{j\omega - a_2} & 0 & 0 \\ 0 & 0 & \frac{j\omega - a_3}{\det(a_{34})} & \frac{a_4}{\det(a_{34})} \\ 0 & 0 & \frac{-a_4}{\det(a_{34})} & \frac{j\omega - a_3}{\det(a_{34})} \end{bmatrix} \tag{29}$$

Where, for simplicity, $$\phi_c = \begin{bmatrix} \phi_{c1} & 0 & 0 & 0 \\ 0 & \phi_{c2} & 0 & 0 \\ 0 & 0 & \phi_{c3} & \phi_{c4} \\ 0 & 0 & -\phi_{c4} & \phi_{c3} \end{bmatrix} = \begin{bmatrix} \phi_{c1} & 0 & 0 \\ 0 & \phi_{c2} & 0 \\ 0 & 0 & \phi_{c34} \end{bmatrix} \tag{30}$$

Since most of the derivatives are zero, we can simplify the equations. Consider the partial derivative of K with respect to the parameters a_{ij} in the real pole case:

$$\frac{\partial K}{\partial a_{11}} = C_c \phi_c \frac{\partial A}{\partial a_{11}} \phi_c B_c = C_c \phi_c \begin{bmatrix} 1 & 0 & 0 & 0 \\ 0 & 0 & 0 & 0 \\ 0 & 0 & 0 & 0 \\ 0 & 0 & 0 & 0 \end{bmatrix} \phi_c B_c = C_c \begin{bmatrix} \phi_{c1}^2 & 0 & 0 \\ 0 & 0 & 0 \\ 0 & 0 & 0 \end{bmatrix} B_c = C_c(:,1)\phi_{c1}^2 B_c \quad (31)$$

In the complex pole pair case:

$$\frac{\partial K}{\partial a_{33}} = C_c \phi_c \begin{bmatrix} 0 & 0 & 0 & 0 \\ 0 & 0 & 0 & 0 \\ 0 & 0 & 1 & 0 \\ 0 & 0 & 0 & 1 \end{bmatrix} \phi_c B_c = C_c \begin{bmatrix} 0 & 0 & 0 \\ 0 & 0 & 0 \\ 0 & 0 & \phi_{c34}^2 \end{bmatrix} B_c = C_c(:,2:3)\phi_{c34}^2 B_c \quad (32)$$

And similarly, with respect to the parameters b_{ij}, c_{ij} and d_{ij} for real poles:

$$\frac{\partial K}{\partial b_{12}} = C_c \phi_c \frac{\partial B_c}{\partial b_{12}} = \phi_{c1}.*C(:,2) \quad (33)$$

$$\frac{\partial K}{\partial c_{12}} = \frac{\partial C_c}{\partial c_{12}} \phi_c B_c = \phi_{c2}.*B(2,:) \quad (34)$$

$$\frac{\partial K}{\partial d_{12}} = \frac{\partial D_c}{\partial d_{12}} = \begin{bmatrix} 0 & 1 \\ 0 & 0 \end{bmatrix} \quad (35)$$

With respect to the parameters b_{ij} and c_{ij} for complex pole pairs:

$$\frac{\partial K}{\partial b_{41}} = \begin{bmatrix} c_{11} & c_{12} & c_{13} & c_{14} \\ c_{21} & c_{22} & c_{23} & c_{24} \end{bmatrix} \begin{bmatrix} \phi_{c1} & 0 & 0 \\ 0 & \phi_{c2} & 0 \\ 0 & 0 & \phi_{c34} \end{bmatrix} \begin{bmatrix} 0 & 0 \\ 0 & 0 \\ 0 & 0 \\ 1 & 0 \end{bmatrix} = \phi_{c4}.*C(:,3) + \phi_{c3}.*C(:,4) \quad (36)$$

$$\frac{\partial K}{\partial c_{14}} = \begin{bmatrix} 0 & 0 & 0 & 1 \\ 0 & 0 & 0 & 0 \end{bmatrix} \begin{bmatrix} \phi_{c1} & 0 & 0 \\ 0 & \phi_{c2} & 0 \\ 0 & 0 & \phi_{c34} \end{bmatrix} \begin{bmatrix} b_{11} & b_{12} \\ b_{21} & b_{22} \\ b_{31} & b_{32} \\ b_{41} & b_{42} \end{bmatrix} = -\phi_{c4}.*B(3,:) + \phi_{c3}.*B(4,:) \quad (37)$$

The simplicity of the derivative matrices allows for numerical efficiency. Matlab code may be obtained in which the general implementation of these calculations is shown.

Now that the partial derivative of K with respect to all parameters has been calculated, it may be substituted back into the gradient of the applicable cost functions. Cost function gradients were defined in reference [1], but the mathematical derivations of these equations were often inexplicit. Re-deriving the gradient equations from the original metrics defined in equations (16) and (18) proved useful. In doing so, the effects of system architecture were made apparent and a typo in reference [1] in the definition of the Critical Point Distance Metric, S_{cr}, gradient was corrected. These detailed derivations can be found in the Appendix.

By simply applying the product rule to equation (16) we have the performance cost gradient:

$$\nabla J_p(p) = \frac{\partial}{\partial p_i} J_p(p) = \frac{2}{\pi} \sum_{k=1}^{len(\omega)} tr\left\{ \mathrm{Re}\left(\left[\frac{\partial}{\partial p_i} H_{cl}(j\omega) \right] H_{cl}^{H}(j\omega) \right) \right\} \Delta\omega \quad (38)$$

To simplify this in terms of the gradient of K, we must first take the partial derivative of H_{cl} which will vary depending on system architecture. Using differentiation by parts on the FSM architecture definition of equation (15), we have:

$$\frac{\partial H_{cl}}{\partial p_i} = SG\frac{\partial K}{\partial p_i} + GK\frac{\partial S}{\partial p_i} \tag{39}$$

The partial derivative of the Sensitivity transfer matrix is also in terms of K and varies depending on system architecture. Using the following rule,

$$\frac{\partial M^{-1}}{\partial p_i} = -M^{-1}\frac{\partial M}{\partial p_i}M^{-1} \tag{40}$$

and letting $M^{-1}=S$ in the FSM architecture definition of equation (14), we have:

$$\frac{\partial S}{\partial p_i} = -S\frac{\partial S^{-1}}{\partial p_i}S = -S\left(\frac{\partial}{\partial p_i}\left(I + GK\right)\right)S = -SG\frac{\partial K}{\partial p_i}S \tag{41}$$

Now it is possible to write the performance cost gradient in terms of the partial derivative of K with respect to the parameters, p.

Derivation and simplification of the gradient of the Critical Point Distance Metric, S_{cr}, is considerably more complex. Recalling the stability metric equations (18) and (19), we have:

$$\nabla S_{cr}(p) = \frac{\partial S_{cr}(p)}{\partial p_i} = \frac{1}{\pi}\sum_{k=1}^{len(\omega)} W_{cr}(\omega_k)\left[\frac{\partial}{\partial p}\frac{1}{d_{cr}^2(j\omega_k)}\right]\Delta\omega_k \tag{42}$$

Equation (43) is the result of letting $M(p)$ equal $(I+F(j\omega))$ from equation (19), where $F(j\omega)$ depends on system architecture. We can use the equation (44) definition of the derivative of a determinant in the case of a non-singular matrix $M(p)$ with distinct eigenvalues:

$$d_{cr}^{2}\left(j\omega_{k}\right)=\det\left(M\left(p\right)\right)\det\left(M\left(p\right)\right)^{H} \tag{43}$$

$$\frac{\partial}{\partial p}\det\left[M\left(p\right)\right]=\det\left[M\left(p\right)\right]tr\left[M\left(p\right)^{-1}\frac{\partial}{\partial p}M\left(p\right)\right] \tag{44}$$

Several additional definitions and properties must be applied to equation (42) in order to define it in terms of the partial derivative of K. One such definition,

$$\frac{\partial K^{H}}{\partial p}=\left(\frac{\partial K}{\partial p}\right)^{H} \tag{45}$$

holds true only if the A_c matrix is symmetrical, which is the case for a modal canonical parameterization. Please refer to the Appendix for the more detailed, architecture dependent, derivations of this gradient.

2.3.5 Tuning

The gradient descent optimization algorithm finds a local minimum of a function, $F(\mathrm{x})$, by taking steps proportional to the negative of the gradient of the function at the current point, x_n. If the function is defined and differentiable in the neighborhood of x_n, then it decreases fastest if one goes from x_n in the direction of the negative gradient of F at x_n. If we define,

$$x_{n+1} = x_n - \gamma_n \nabla F(x_n) \tag{46}$$

for step size γ_n>0 a small enough number, then $F(x_n) \geq F(x_{n+1})$. The value of the step size is allowed to change at each iteration. The algorithm can take an arbitrary number of iterations to converge, but there is a variable that allows one to limit the total allowable number of iterations in this algorithm in the interest of time. Finding the optimal step size each iteration can also be time-consuming but using a fixed step size can produce poor results. There are many techniques that may be used for determining step size. Once determined, the step size can be further limited by the algorithm with closed-loop and compensator stability checks. The technique suggested by reference [1] for the stepping algorithm is the iterative Boyden-Fletcher-Goldfard-Shanno (BFGS) nonlinear descent method which requires that the gradient of the cost be computed at arbitrary points using the expressions defined in 0. Reference [1] prefers BFGS over other descent methods based on informal comparison of performance and computational complexity with the developed tuning algorithms and an additional similar study.

In order to simplify the tuning process, BFGS was not used in the initial algorithm development. Rather, the step size was set to an initial value of one and allowed to be halved if it produced a tuned compensator that did not satisfy the algorithms stability checks, which are detailed in section 2.3.6.

2.3.6 Stability Determination

In the case of the DOT structure, preserving open loop (OL) and closed loop (CL) stability is desired. Since the compensator is always available in state-space form, its

stability is ensured by simply confirming the eigenvalues of A_c are inside the unit circle. If the plant is OL stable, which it is for all cases examined in this thesis, and the compensator has been shown to be OL stable, it follows that the system is OL stable. Determining CL stability when only frequency response data is available to define the plant is more complex. A knowledge-based algorithm is developed in reference [1] to automatically implement the rules of the MIMO stability criterion to determine stability.

Recall equation (19) and its dependence on system architecture. The MIMO Nyquist function can be determined at each frequency point:

$$L(j\omega) = -1 + \det(I + F(j\omega)) \tag{47}$$

The MIMO Nyquist stability requires that the net number of counter-clockwise (CCW) encirclements of the critical point, -1 in the case of equation (47), made by the locus of $L(j\omega)$ on the complex plane must be equal to the number of unstable poles in the OL system [4]. It is simpler to quantify this in an algorithm by employing the Nichols plot where the locus of $L(j\omega)$ is plotted as log-magnitude versus phase [7]. In this form, encirclements in the Nyquist plot are equivalent to passes of the locus of $L(j\omega)$ over the critical points at a magnitude of one with phase $-180 \pm n360$ degrees. Thus the net number of left to right (lower to higher phase) passes of the locus of $L(j\omega)$ over the critical points must be equal to the number of unstable poles in the OL system.

$L(j\omega)$ points are placed in their respective quadrants according to the following figure:

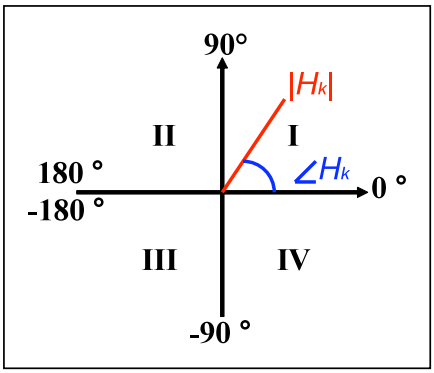

Figure 5. Quadrant Definition for CL Stability Determination

Subsequent points, $L(j\omega_k)$ and $L(j\omega_{k+1})$, are compared and a right to left pass of a critical point corresponds to traversing from quadrant three to two (clockwise). A left to right pass corresponds to traversing from quadrant two to quadrant three (counter-clockwise). Encirclements are counted only for subsequent points whose corresponding magnitudes are greater than one.

In the case where there is a quadrant two to three or three to two crossover and only one magnitude is greater than unity, then it is unclear if the locus has passed over or under the critical point. Linear interpolation to generate points between ω_k and ω_{k+1} is recommended, but a more conservative and less computational approach is to go ahead and count this case as an encirclement.

In the case where consecutive points skip a quadrant (one to three, two to four or vice versa) and the magnitude of the points exceeds unity, data is considered to be bad (noisy and/or sparse). This case proves to be rather problematic in the implementation of the algorithm with noisy and/or sparse Digital Signal Analyzer (DSA) frequency response data and is discussed in more detail in section 3.2.

As stated earlier, with a passive plant we can assume the plant is OL stable meaning there are no right half plane (RHP) poles. In the case that the tuned state-space compensator is OL stable (which is the first criteria to be satisfied in the algorithm), meaning there are no RHP poles; a CW encirclement of the critical point by the locus indicates a zero in the RHP and thus an unstable root of the CL system. Therefore, the criteria for confirming the tuned compensator stabilizes the plant is based on MIMO Nyquist locus having zero CW encirclements of the critical point – we need not concern ourselves with counting CW and CCW encirclements, only detecting if any CW encirclements exist.

Please compare the following two figures which show an example of the MIMO Nyquist and MIMO Nichols plots, respectively, for the FSM structure from 140 to 2000 Hertz. The red lines show smooth data and the blue show the true noisy data. The MIMO Nyquist data begins at 140 Hertz in the south-east corner of Figure 6 and that corresponds to the point of greatest magnitude in Figure 7. Observe the green asterisk in the figures; note the jump from quadrant two to three (left to right) in Figure 7 and how it corresponds to the CCW pass around the critical point in Figure 6. Similarly, the cyan asterisk corresponds to a jump from quadrant three to two (right to left) and a corresponding CW pass of the critical point. However, one will observe the magnitude of the right to left pass is less than one, meaning it does not get included in the net encirclement summation.

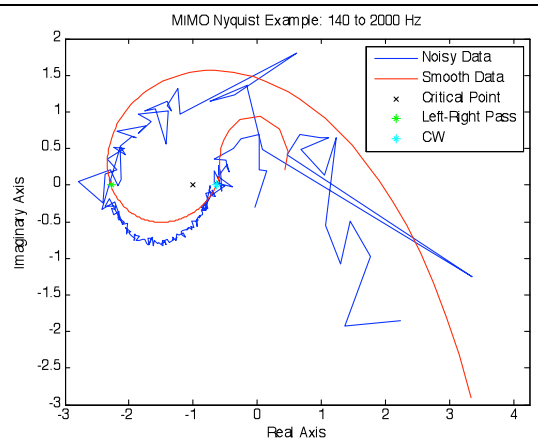

Figure 6. MIMO Nyquist Example

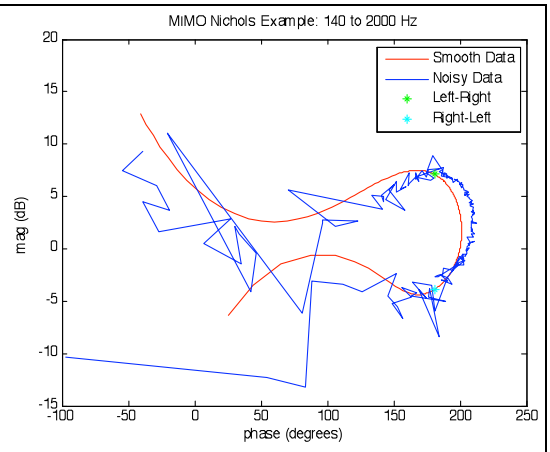

Figure 7. MIMO Nichols Example

Preserving stability is what makes the tuned compensator so dependent on the baseline compensator. It ensures all iterations occur within the stable set containing the baseline compensator. There may be an alternate stabilizing set of compensators corresponding to clockwise/counter-clockwise encirclement cancellation that the algorithm never approaches. However, allowing the algorithm to search for that alternate set of stable compensators may result in a vastly more complex algorithm.

2.4 Summary

This chapter has described the algorithm, as developed in reference [1], and its applied components in this thesis. The following chapter will expand on the components that were extended and/or modified for use with noisy FRF and uncertainty data from a MIMO system.

CHAPTER 3 CONTRIBUTIONS

In the implementation of the algorithm presented in references [1] and [2], some modifications and/or extensions have been considered in the case that MIMO uncertainty data is available and FRF data is noisy.

3.1 Stability Cost Function

It is mentioned in reference [1] that the MIMO Nyquist criterion is a necessary but not a sufficient condition for determining stability because the properties of the determinant operator are problematic. Thus the sensitivity singular value cost is proposed as a complementary stability robustness measure. However the problematic properties of the determinant only apply to cases of structured uncertainty. Because the MIMO Nyquist criterion is based on the small gain theorem [8], it is both necessary and sufficient for determining stability robustness if the plant perturbations are unstructured. For this application our focus is on unstructured uncertainty, that is the frequency response uncertainty, and the complimentary sensitivity cost S_s is ignored:

$$J_s(p) = S_{cr}(p) \tag{48}$$

Recall the definition of S_{cr} from equation (18). One interesting component is the $W_{cr}(\omega_k)$ term. It is defined in reference [1] as a vector weighting function on the frequency values of interest, which also weights the relative contribution of the stability cost to the total cost. It can be used to push important frequency points away from the critical point. In reference [2], the standard deviation of the frequency response data for a single-input, single-output (SISO) system is available and used to define this weighting term. Because

in the SISO case the standard deviation associated with each frequency of the frequency response data is a scalar, d_{cr} was defined as:

$$d_{cr}(j\omega) = \frac{\det(I + F(j\omega))}{\sigma(j\omega)} \tag{49}$$

And thus

$$\frac{1}{d_{cr}^2(j\omega)} = \frac{\sigma^2}{[\det(I - F(j\omega))][\det(I - F(j\omega))]^H} \tag{50}$$

Where σ^2 is the variance of the FRF data and can be pulled out and considered as part of the weighting function, $W_{cr}(\omega_k)$. This stability cost definition ensures that the cost function will decrease as the curve moves farther from the critical point and/or has a smaller variance. However, in the MIMO case, the variance data is a matrix and must be properly propagated from its matrix FRF form to the Nyquist curve; a scalar due to the use of the determinant operator of the Multivariable Nyquist criterion.

Two options have been considered for reducing the variance matrix to a scalar value. The first is an H_2 norm approach, taking the maximum value of the variance matrix at each frequency point of interest. The second, less conservative, approach is based on treating the variance as a random variable with a given distribution**.** It is possible to approximate the distribution of a nonlinear function of a random variable by linearizing the function about the mean of the variance data, so that the standard deviation of the nonlinear function of the variance is just a scaled version of the square-root of the variance. Note when the function is highly nonlinear, has a large second derivative, compared to the standard deviation of the data, this approach does not work well.

The linearization approach is derived as follows:

Let $$W_{cr}(\omega_k) = \sigma_{nyq}^2 \tag{51}$$

Where $$\sigma_{nyq} = \frac{\partial d}{\partial G}\sigma_G \tag{52}$$

And σ_G is the standard deviation of the FRF data,

Then
$$\begin{aligned}\sigma_{nyq} &= \frac{\partial}{\partial G}\left|\det\left(I + F(j\omega)\right)\right|\sigma_G \\ &= \frac{\partial}{\partial G}\left[\det\left(I + F(j\omega)\right) * \det\left(\left(I + F(j\omega)\right)^H\right)\right]^{/2}\end{aligned} \tag{53}$$

The verdict is still out on whether equation (53) is differentiable or not. If it is differentiable, the result is expected to still be a matrix, so the inner product must be taken to get a scalar:

And $$\sigma_{nyq} = \left\langle \frac{\partial d}{\partial G}, \sigma_G \right\rangle \tag{54}$$

If DSA measured variance data has anomalous data, those frequency points should be removed. If that leads to a sparse data set in regions of interest, one may precondition the variance data to be no greater than the gain of the system at applicable frequency points.

3.2 Stability Determination

In section 2.3.6, the negative effects of noisy DSA data on the CL Stability Check algorithm were mentioned. During algorithm development, it was found that the phase of the Multivariable Nyquist locus created using DSA data did not align with that created

using the pristine simulation data, see Figure 8. The determinant of (I+GK) where the FRF data of the plant G had been created from the noisy magnitude and phase of the DSA data, could not be reliably transferred back again to a representative phase because of the magnification of the noise resulting from taking the determinant. Thus a discrepancy was seen in the CL stability algorithm, allowing it to identify an unstable system as stable.

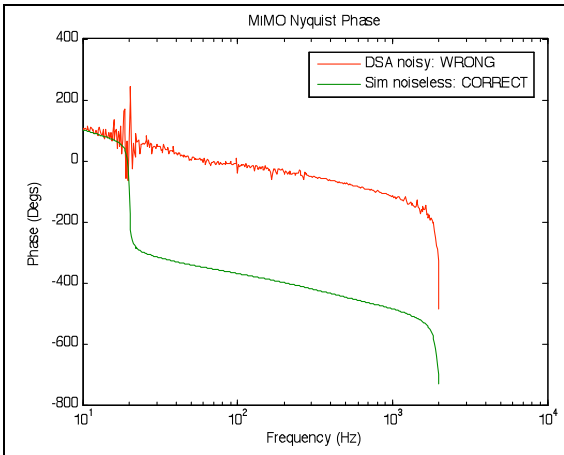

Figure 8. Incorrect MIMO Nyquist Phase

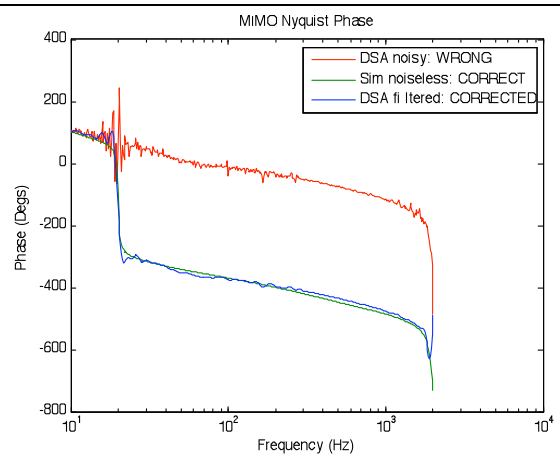

Figure 9. Corrected MIMO Nyquist Phase

The selected solution is to filter the DSA magnitude and phase data before it is transformed into the FRF format. A method consisting of using a running average with variable window size based on DSA variance data was considered, but that method has a tendency to introduce lag into the magnitude and phase. Therefore, the data is instead filtered using Matlabs *filtfilt* function which performs zero-phase digital filtering by processing the input data in both the forward and reverse directions, it additionally attempts to minimize startup and ending transients by matching initial conditions. This

filtered plant FRF data was used only in the CL stability determination algorithm, see Figure 9.

3.3 Summary

This chapter has shown how the algorithm can be modified and extended for use with MIMO uncertainty data and noisy FRF data. The following chapter describes how the algorithm with its modification and extensions was implemented using actual MIMO FRF and uncertainty data. It also shows the results of that implementation.

CHAPTER 4 IMPLEMENTATION

This chapter will discuss how the previously described algorithm is applied to a specific model. The results of this application will demonstrate its performance and viability for use with other, similar systems.

4.1 Algorithm Flow Chart

The flow chart in Figure 10 outlines how the algorithm was implemented in Matlab code:

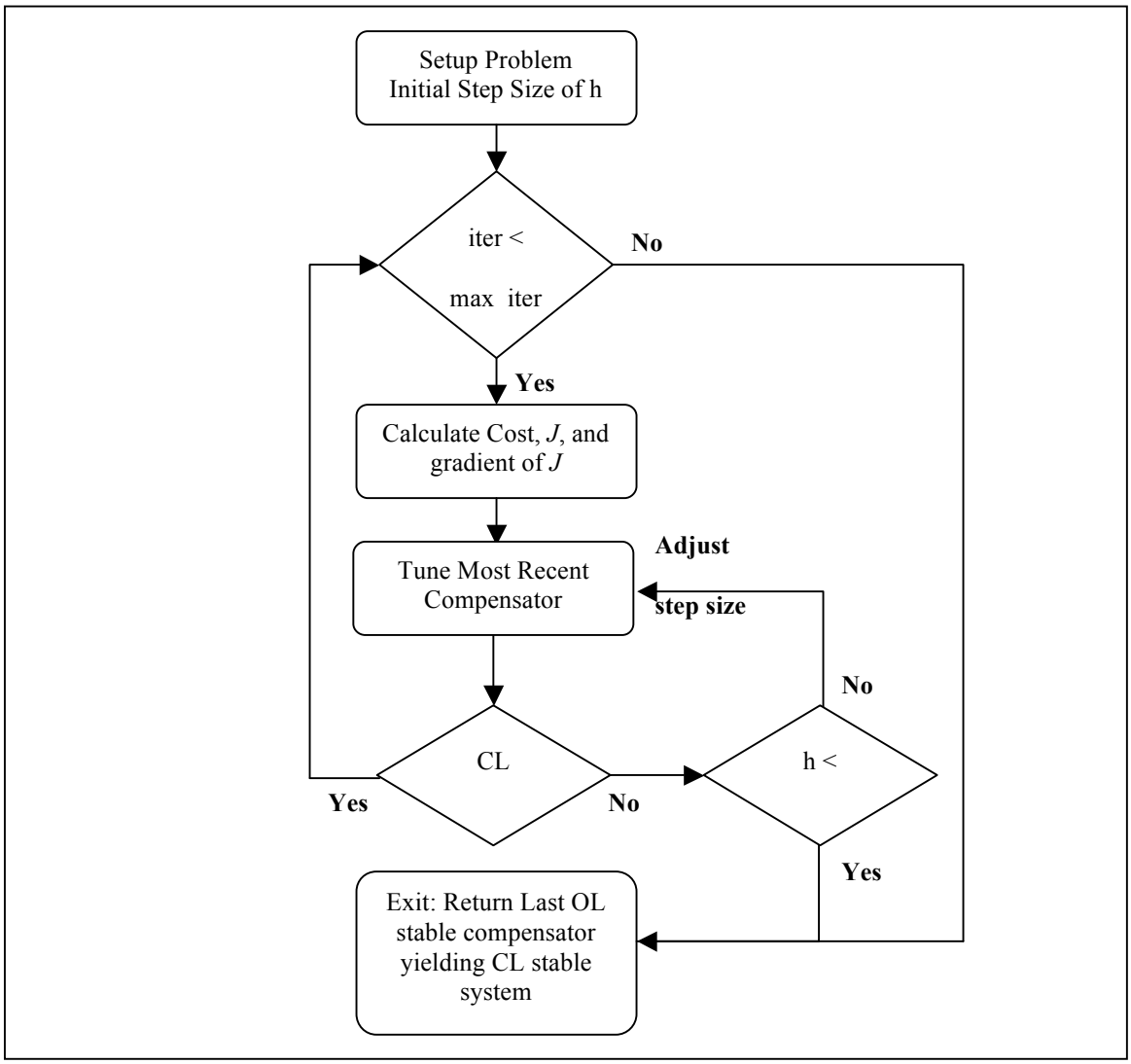

Figure 10. Flow chart of applied algorithm.

4.2 System Overview

4.2.1 The DOT Structure

For a detailed description of the DOT structure and design, refer to reference [3]. The DOT structure is a 10 input, 9 output MIMO system with 334 states. Frequency response functions are acquired between optical outputs of tip, tilt and piston of each primary mirror segment, and the ten actuators in the system. It is an open-loop stable structure. The baseline controller was created from a system identification performed on the un-cabled DOT structure. Since that time, cables have been added to the structure and new frequency response data has been collected. To simplify the calculations and time required to run the algorithm, the DOT structure was reduced to a single petal, 3x3, system and the order of the compensator was reduced from 344 to 40 states using model truncation on the balanced realization. The compensator was developed using the LQG method.

Originally, the architecture was simplified and the integral action was omitted. A block diagram of the original architecture is shown in Figure 11 and a suggested architecture is shown in Figure 12. The suggested architecture includes the integral action as part of the plant, thus removing it from the compensator state space matrices that are tuned by the optimization algorithm and preventing its potential elimination during tuning.

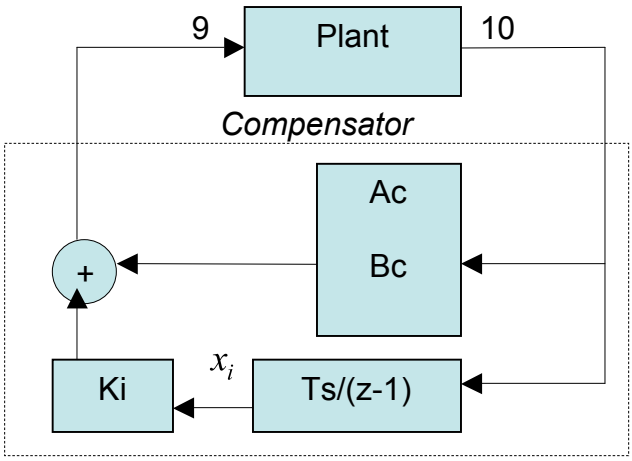

Figure 11. Current System Configuration

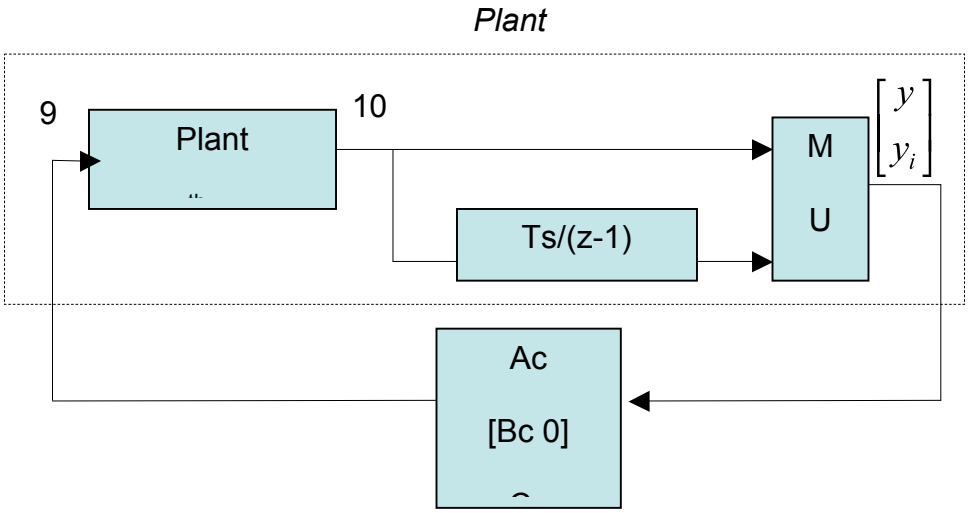

Figure 12. Suggested System Configuration

4.2.2 The FSM Structure

The FSM structure consists of independent, but equivalent, X and Y axis second order SISO compensators with integral action. X and Y outputs are passed through a decoupling matrix yielding three outputs corresponding to the FSM's three coil structure. Thus, for the purposes of exercising this optimization algorithm, the compensator is

turned into a two input, three output MIMO system which includes the decoupling matrix. The plant is therefore represented as a three input, two output MIMO system, Figure 13, that includes the power amplifiers and coupling matrices that feed X and Y acceleration to the FSM dynamics model shown in Figure 14.

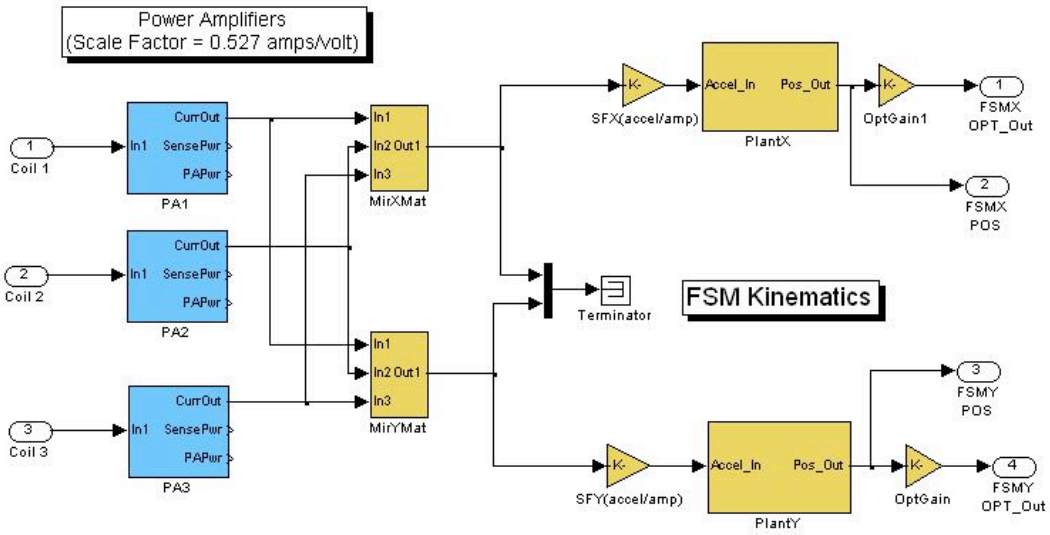

Figure 13. 3x2 MIMO Plant

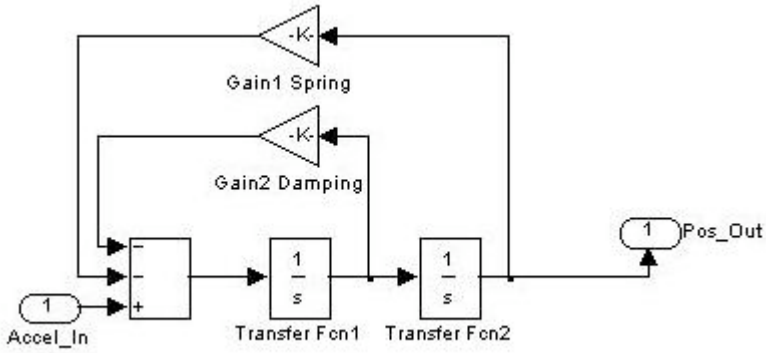

Figure 14. FSM Dynamics

Figure 15 shows a model of the entire CL system. The plant is OL stable. The modeled compensator was developed using classical control techniques and has no complex poles.

Appropriate filters were added later to the actual system after system dynamics were analyzed. Frequency response data was collected with a Digital Signal Analyzer for the X and Y axes of the OL system. Y axis data is shown in Figure 16.

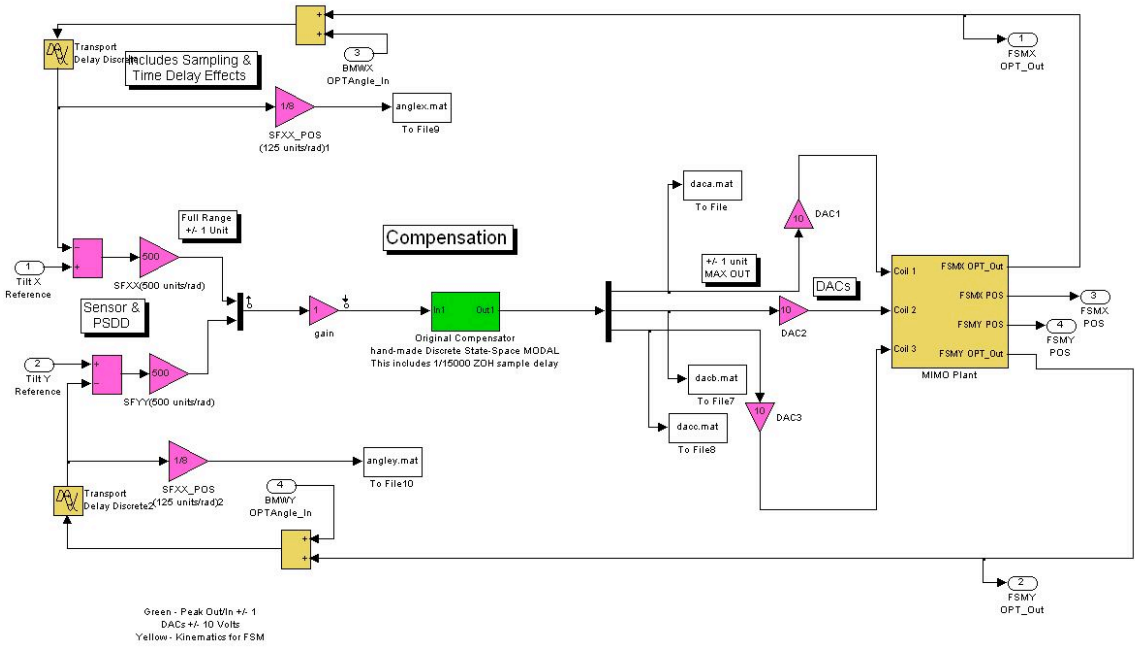

Figure 15. CL FSM System

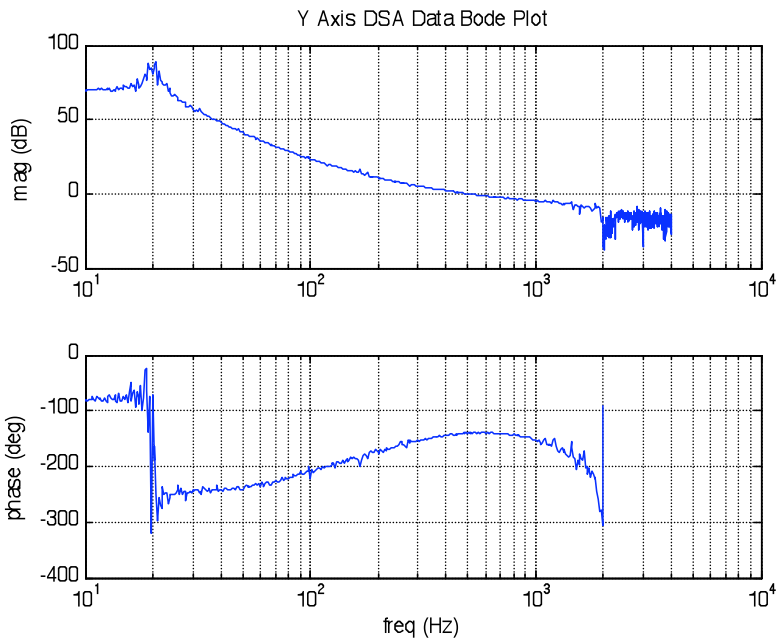

Figure 16. Y Axis DSA Data Bode Plot

Since the FRF data included the compensation, it had to be defined and removed so that the three input, two output plant FRF data remained for use in the algorithm Variance data was not collected with the FRF data and was heuristically defined by applying a best fit to the data, normalizing it and squaring the running standard deviation. This data is shown in Figure 17.

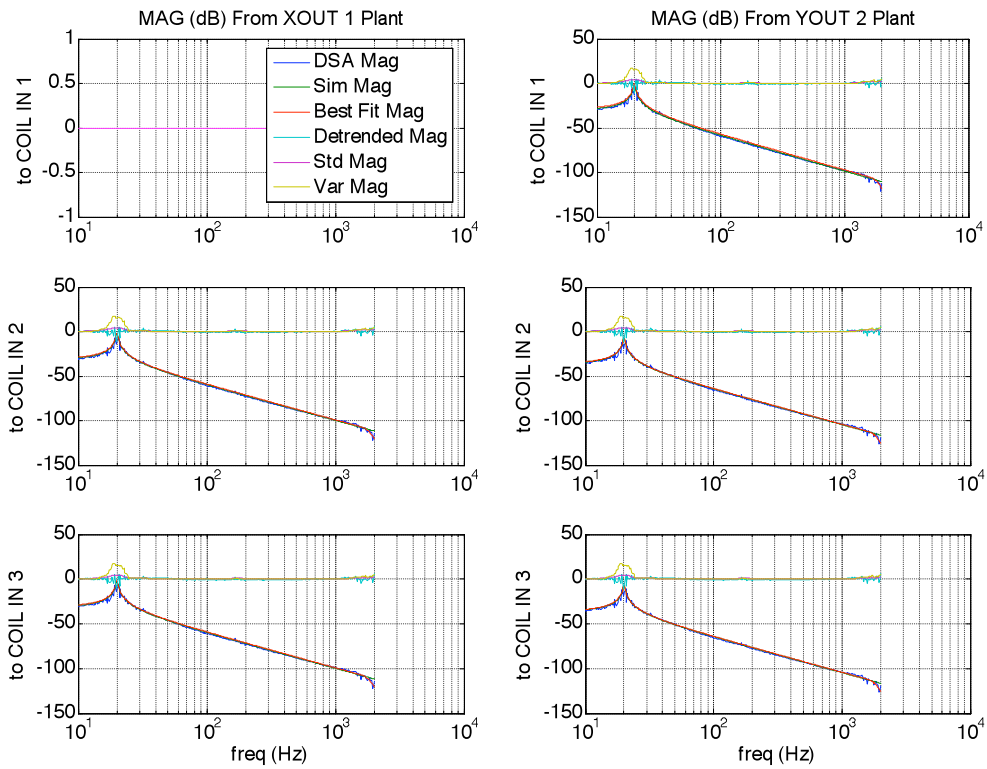

Figure 17. 3x2 Plant Using DSA Data

4.2.3 Order of Implementation

Perhaps too ambitiously, the algorithm was first applied to a reduced order DOT model. This produced some very thought provoking results, but proved to be rather difficult to debug due to the complexity of the system. Thus, a simpler model was reverted to for easier algorithm verification. Understanding how the algorithm performs with a simpler system will help determine its strengths and weaknesses and if it is a viable option for use with the DOT system.

4.3 Results of Algorithm Application to the FSM Structure

4.3.1 FSM Cases Tested with the Tuning Algorithm

The compensation used in the simulation was designed classically and has no complex poles. This compensation was first used in the optimization algorithm and results did not show much of an improvement. One might assume, if the algorithm is working properly, that this particular compensator cannot be improved upon in its current form; that is, the optimization routine implemented does not augment the compensator size or increase the number of complex poles. It was necessary to give the optimization routine more to work with by having it tune the actual compensator, which includes the complex poles associated with the added notch filters. Results of tuning the actual compensator verified that the optimization routine was working as designed. The simplicity of the FSM system, the X and Y axes being uncoupled, allows us to look at the bode plots of the system to understand stability and performance in addition to the Multivariable Nyquist plot, which can be a less intuitive indicator.

In addition to giving the optimization algorithm different compensators to tune, one can vary the stability and performance cost weighting value, alpha. Recall alpha from equation (20). A value of one for alpha means the optimization algorithm tunes based only on minimizing the performance cost. Alternately, a value of zero for alpha means the optimization algorithm tunes based only on minimizing the stability cost. Thus, with a value of one for alpha, we expect to see an improvement in the system performance, but not necessarily in the system stability, and vise versa.

One may recall, from section 2.3.3, that precautions must be taken to preserve integral action during the tuning process. Observe a 9x9 section of the actual 18x18 FSM compensator discrete state-space *A* matrix, in Modal Canonical form, in Figure 18. This is a discrete compensator. Element [7,7] represents the integral action for the X axis. Element [16,16] of the full 18x18 FSM compensator discrete state-space A matrix, viewable in the appendix , represent the integral action for the Y axis. To avoid the possibility of the tuning algorithm reducing these elements to zero, thus eliminating the integral action, these elements are removed from the parameter list during the tuning process.

0.5865	0.7726	0	0	0	0	0	0	0
-0.7726	0.5865	0	0	0	0	0	0	0
0	0	0.5961	0.7652	0	0	0	0	0
0	0	-0.7652	0.5961	0	0	0	0	0
0	0	0	0	0.6646	0.6988	0	0	0
0	0	0	0	-0.6988	0.6646	0	0	0
0	0	0	0	0	0	1.0000	0	0
0	0	0	0	0	0	0	0.6477	0.0026
0	0	0	0	0	0	0	-0.0026	0.6477

Figure 18. Subset of the Discrete State-Space *A* Matrix of the Actual FSM Compensator

Results shown in Figures 19 through 23 are using the actual compensator and an alpha of zero, meaning the optimization algorithm is minimizing the stability cost. Therefore, a plot of the stability and performance costs should show a decrease in the stability cost, though not necessarily a decrease in the performance cost. Figure 19 shows that both the stability and performance costs were improved. Recalling equation (18), we expect to see the tuning result in an increase in the distance of the MIMO Nyquist from the critical point. Figure 21, a zoom on the critical point of the MIMO Nyquist plots in Figure 20,

shows that this is occurring as the algorithm goes through its iterations. The step size, h, started out at a value of one, but when iteration three produced an unstable system (the dotted green line in Figure 20), the step size was halved, and would have continued to be halved until a stable system was produced. It is apparent from both Figure 19 and 20 that the algorithm begins to converge after iteration three; stable results from iterations three through five are nearly overlaid.

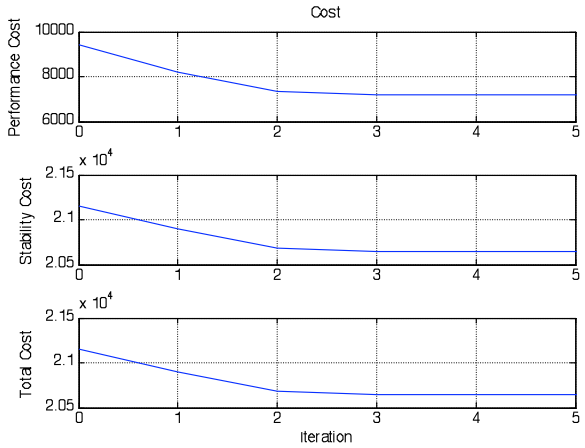

Figure 19. Cost Function Progression for Stability Optimization

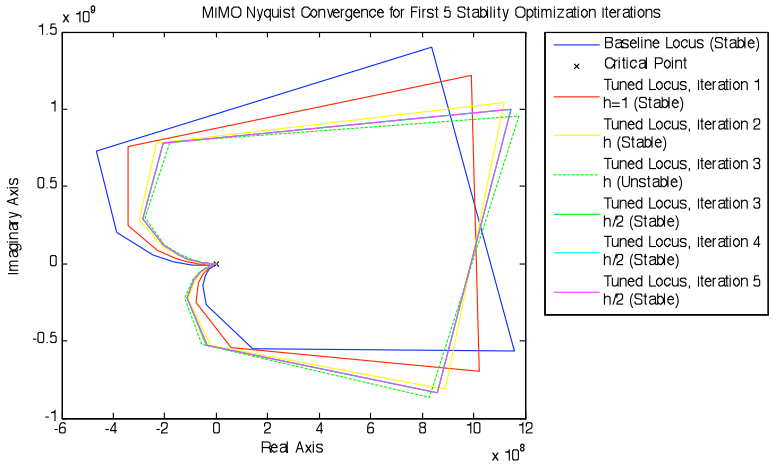

Figure 20. MIMO Nyquist Convergence for Stability Optimization

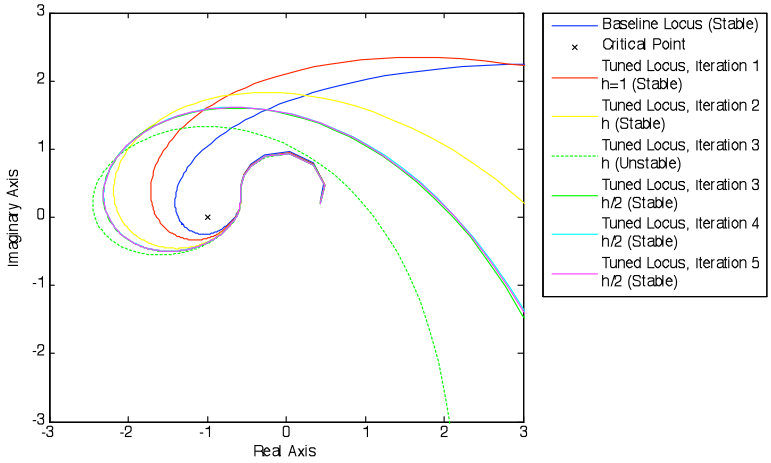

Figure 21. Zoom of MIMO Nyquist Convergence for Stability Optimization

The improvement in the stability is obvious when looking at a single axis bode plot, shown in Figure 22. The baseline OL DSA data system (dark green dashed) has a bandwidth of ~500 Hz with a corresponding phase margin of ~40 degrees. The tuned OL DSA data system (light green solid) has a bandwidth of ~475 Hz with a corresponding phase margin of ~60 degrees. The performance cost function indicated that system performance had also improved, though only stability cost was minimized during

optimization. At first glance, it is not apparent how the performance has been improved. In fact, due to the obvious loss of error rejection at frequencies below cross over (tuned magenta versus baseline red sensitivity), it seems the performance cost improvement must be erroneous. However, one must remember the algorithm is only doing what it has been told to do. Zooming in on the sensitivity curve, Figure 23, reveals that the overshoot of the error rejection has been reduced. The performance cost function registers this as an improvement in spite of the loss of error rejection at lower frequencies.

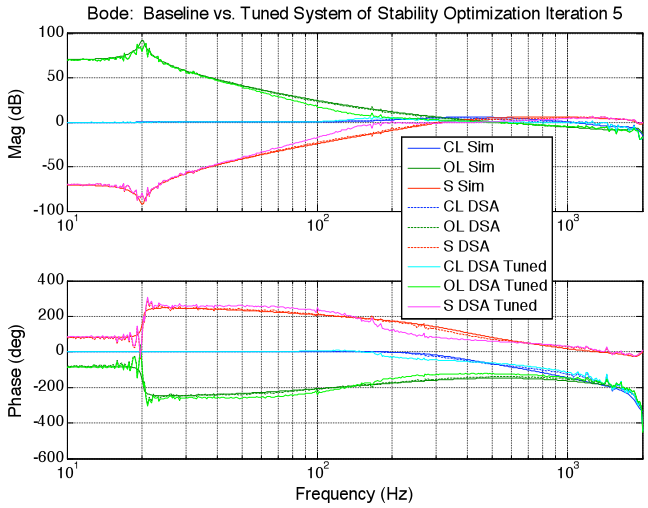

Figure 22. Bode Plot for Stability Optimization

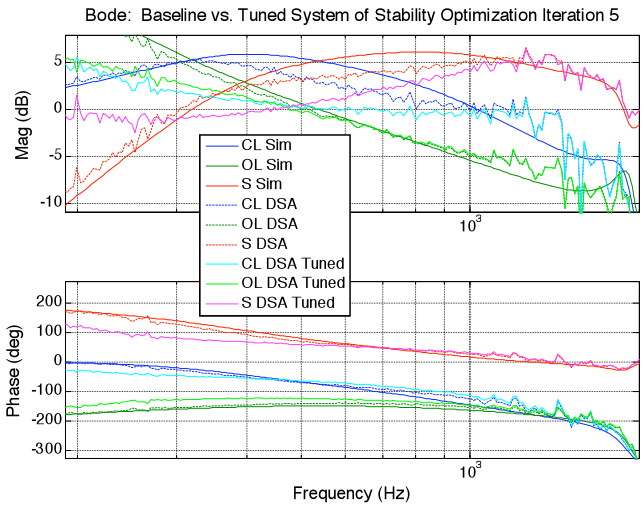

Figure 23. Zoom of Bode Plot for Stability Optimization

The optimization algorithm was rerun with alpha set to one, meaning the optimization algorithm is minimizing the performance cost. Therefore, a plot of the stability and performance costs should show a decrease in the performance cost, though not necessarily a decrease in the stability cost. The plot of the cost function values throughout the iterations is shown in Figure 24 and indicates that the values for both Performance and stability are decreasing and they converge on similar values to those seen in Figure 19, one difference being that it took fewer iterations to converge. Also, Figure 25 indicates that the step size had to be reduced greatly for the compensator tuning to arrive at a stable system. Figures 24 through 27 show that the final system is nearly identical to that converged upon when the stability cost function was being minimized.

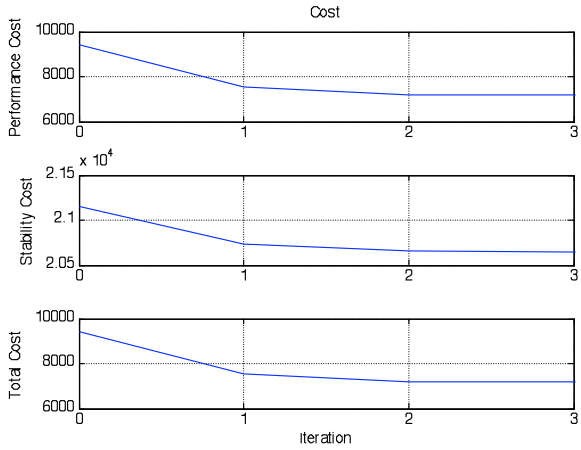

Figure 24. Cost Function Progression for Performance Optimization

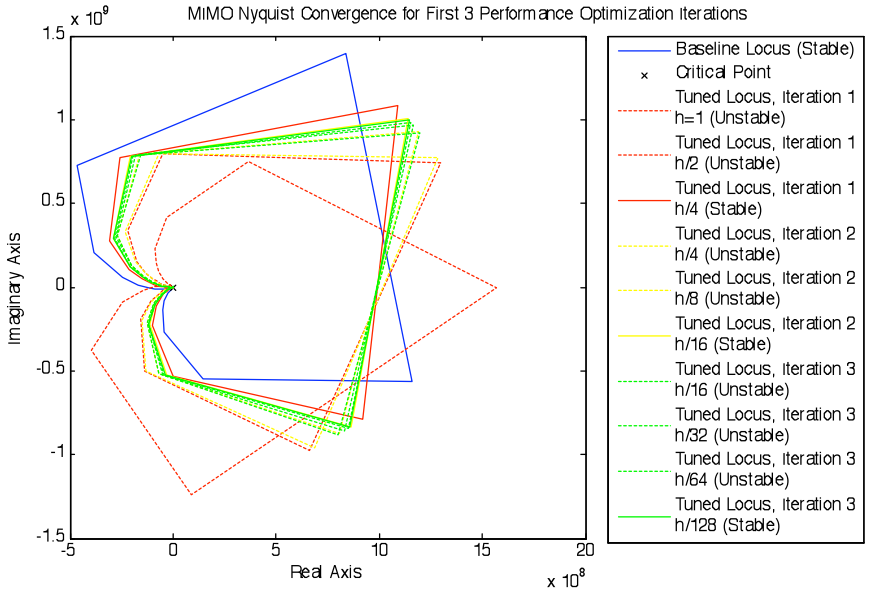

Figure 25. MIMO Nyquist Convergence for Performance Optimization

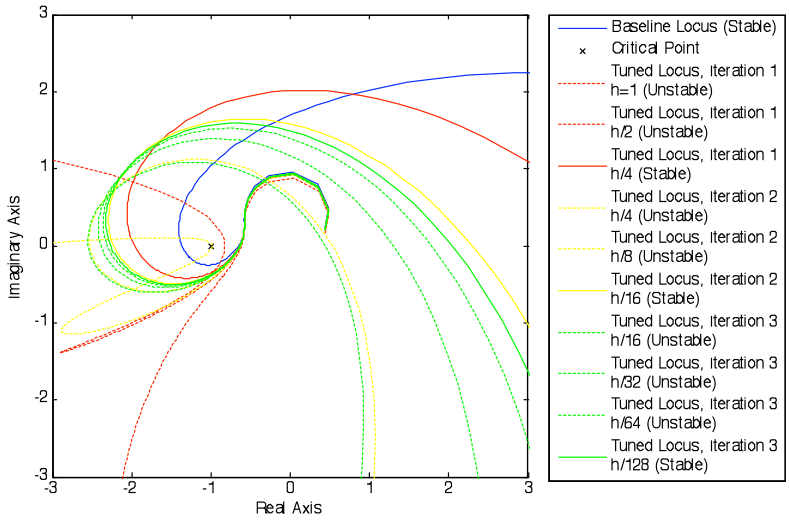

Figure 26. Zoom of MIMO Nyquist Convergence for Performance Optimization

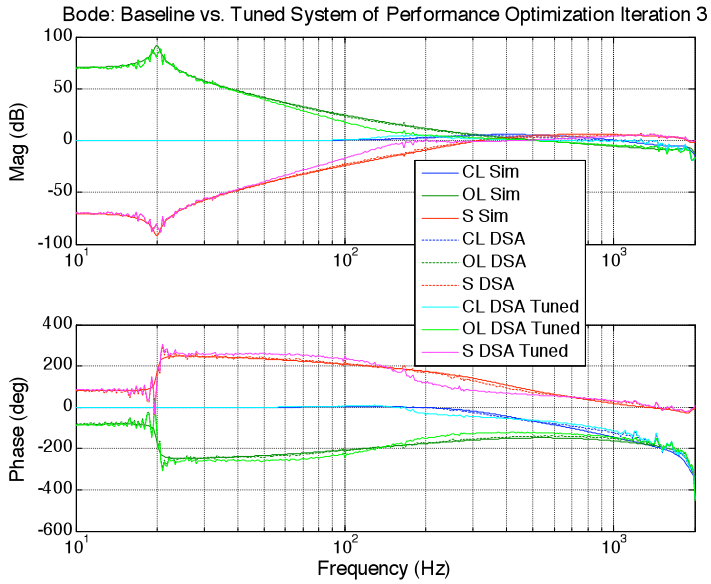

Figure 27. Bode Plot for Performance Optimization

In order to help the performance cost function improve performance in a frequency area of interest, in this case the error rejection at lower frequency, we can apply a performance cost weighting variable. The optimization algorithm was rerun with alpha set to one,

minimizing performance cost only, with a weighting vector the same length as the frequency vector. The weighting vector consisted of ones below the 200Hz index and zeros above the 200Hz index; the weighting vector could be any function that appropriately suits the desired performance improvement. The cost over the iterations, Figure 28, shows that the performance cost improved but at the expense of the stability cost.

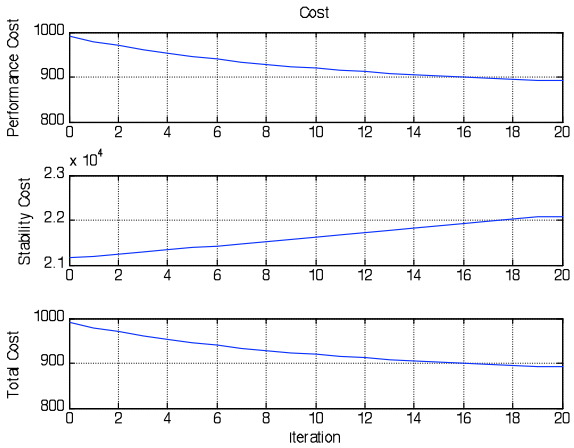

Figure 28. Cost Function Progression for Weighted Performance Optimization

You can see how the MIMO Nyquist locus moved closer to the critical point in Figure 30 indicating a less stable system according to the stability cost function. It took more iterations to converge than the previous performance cost took and the step size never needed to be reduced from its original value of one.

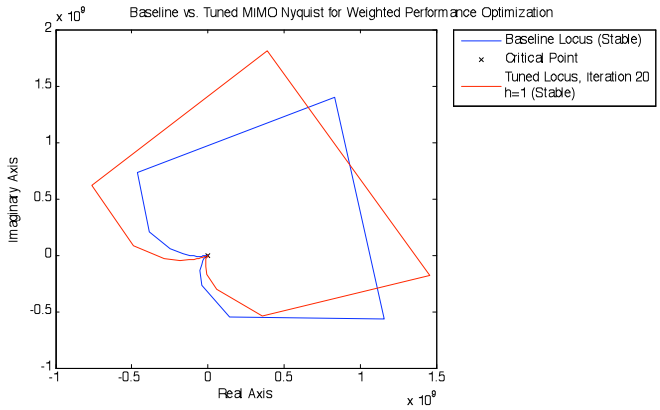

Figure 29. MIMO Nyquist Convergence for Weighted Performance Optimization

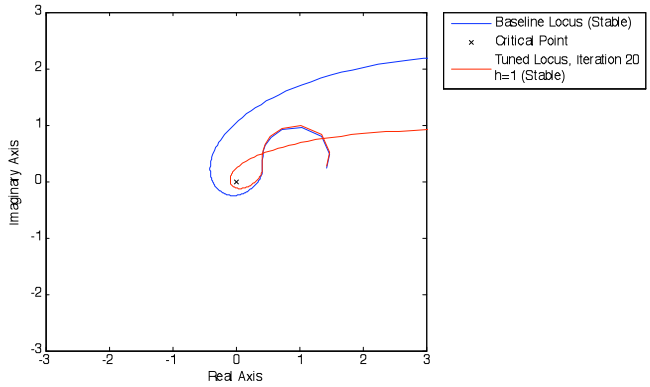

Figure 30. Zoom of MIMO Nyquist Convergence

for Weighted Performance Optimization

Looking at the single axis bode plot in Figure 31 shows the performance weighting had the desired affect on the performance optimization, increasing the error rejection at lower frequency (the magenta versus the red lines). Figure 31 also shows how the stability was reduced. The baseline OL DSA data system (dark green dashed) has a bandwidth of ~500 Hz with a corresponding phase margin of ~40 degrees. The tuned OL DSA data system (light green solid) has a bandwidth of ~575 Hz with a corresponding phase margin of ~25 degrees.

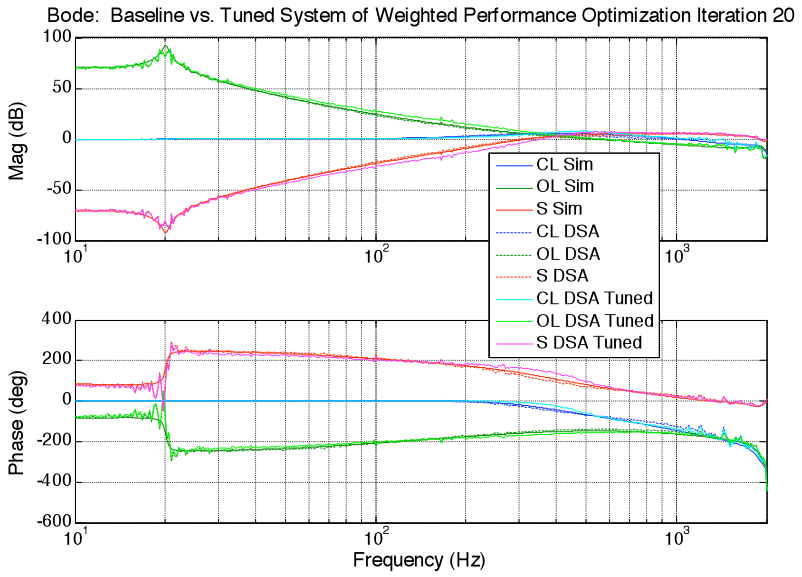

Figure 31. Bode Plot for Weighted Performance Optimization

With this newly defined performance cost weighting in place, if the optimization algorithm is rerun for an alpha of zero, minimizing stability cost, we would no longer see the performance cost improve as we did in Figure 19. This is demonstrated in Figure 32.

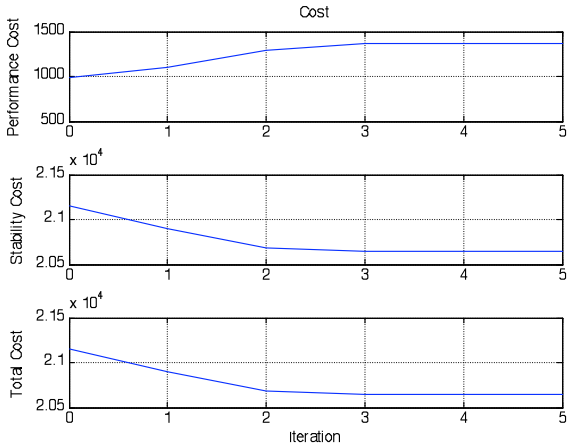

Figure 32. Cost Function Progression for Stability

Optimization and Weighted Performance

Now one may vary the alpha weighting on the performance and stability cost according to what type of improvement is desired.

Recall the discussion in section 3.1 about the use of the FRF uncertainty, in the form of the variance of the FRF data, in the stability cost function. It was intended that the conservatism of the MIMO Nyquist locus as a measure of robustness be countered by the inclusion of the FRF uncertainty in the stability cost function. To verify that this modification was successful, the weighting term which was a function of the FRF variance data, was removed from the stability cost function and the optimization algorithm was rerun with alpha equal to zero; minimizing the stability cost only. Results showed that the compensator tuning converged on the same compensator produced by running the optimization routine with the stability weighting in place, depicted in Figures 20 through 23. The difference was that, because the stability metric was more

conservative without the stability weighting in place, it took more iterations to converge on this compensator.

4.4 Results of Algorithm Application to the DOT Structure

4.4.1 DOT Cases Tested with the Tuning Algorithm

As stated in section 4.2.3 the complexity of the DOT structure made it hard to debug the algorithm and the simpler FSM system was reverted to. Unlike the FSM system, the DOT system had variance data that was collected by the DSA. It was discovered the variance data exhibited some anomalies where the measured variance was either not a number (NaN) or excessively large. This was an artifact of the FRF data collection approach. Since these anomalous values adversely affected the weighting for the stability cost function, they were either removed from the FRF set or preconditioned not to exceed the gain of the system.

4.5 Summary

This chapter demonstrated the optimization algorithm's effect on compensator stability and performance as well as the algorithm improvement due to the inclusion of uncertainty data. Because is performed as expected, it appears a viable algorithm to apply to the DOT structure and other similar systems.

CHAPTER 5 CONCLUSIONS

As is often the case, the step from theoretical to practical application proves challenging. Dealing with the nuances of noisy data can be quite frustrating and was one of the greatest obstacles to a robustly functioning optimization algorithm. As indicated earlier, noisy data can lead to false stability checks if not dealt with properly. It can also dramatically affect the cost functions and their gradients, and subsequently the entire tuning of the compensator. There are numerous parameters and variables to be considered in the definition and tuning of a compensator. Algorithm simplicity, for ease of algorithm validation and confidence, must be balanced with algorithm complexity, necessary to produce optimal results; and this balance is best achieved by one with a thorough knowledge of the system and its dynamics.

A main goal of investigating the application of the optimization algorithm presented in reference [1] was to understand its viability, specifically in the case of the Deployable Optical Telescope systems and systems like it. The above analysis has demonstrated that the algorithm, when applied knowledgably, can produce an improved compensator when given a non-ideal compensator to tune and measured FRF data to accompany it. With an extensive understanding of the system specific dynamics and noise, this optimization algorithm has the potential to be a very efficient and helpful tool for complex MIMO systems operating in remote and varying conditions.

Areas recommended for future work in reference [1] which were addressed in this thesis include:

- Exploration of the connection between the stability robustness metric and model uncertainty: The plant model variance data was incorporated into the stability cost function and its inclusion demonstrated improvement of the optimization in that it took fewer iterations to converge.
- The development and implementation of the tuning methodology in the discrete-domain as opposed to the continuous domain: In reference [1] compensators were tuned in the continuous-time domain and converted to discrete-time compensators, whereas this algorithm directly tuned discrete-time compensators.

The Tuning Algorithm should be tested on various other systems, including several cases of the DOT structure. Once the scripts are adequately validated, progress using the cabled DOT FRF data can be made and ultimately a tuned controller applied to the actual DOT cabled structure.

There are many other useful paths that should be explored. They include:

- The identification of relevant frequency information, log versus linear down-sampling of frequency vector.
- Further research into the gradient descent algorithm regarding its extension to finding global versus local minima.
- Proper tuning of the performance and stability weighting factors.
- What to do in the case that the plant is not open loop stable.
- Advantages/Disadvantages of limiting the optimization iterations and step sizes by requiring open loop and closed loop stability at every iteration.

Overall, the algorithm is promising and further development could yield an extremely useful adaptive control algorithm.

APPENDIX A

STABILITY ROBUSTNESS DERIVATIVE CALCULATION

Calculations were aided by identities and equations found in reference [5].

Let $$M(p) = (I + F(j\omega))$$

Then $$d_{cr}^2(j\omega) = \frac{[\det(M(p))][\det(M(p))]^H}{\sigma^2}$$

Recall equation (42) defining the gradient of the Stability Cost Function. It requires that we calculate:

$$\frac{\partial}{\partial p}\frac{1}{d_{cr}^2(j\omega_k)} = \frac{\partial}{\partial p}\frac{\sigma^2}{[\det(M(p))][\det(M(p))]^H}$$

Let $$a = \det(M(p)),\ b = [\det(M(p))]^H,\ D = ab$$

Then $$\frac{\partial}{\partial p}\frac{\sigma^2}{D} = \frac{-\sigma^2}{D^2}\frac{\partial D}{\partial p} = \frac{-\sigma^2}{D^2}\left(\frac{\partial a}{\partial p}b + \frac{\partial b}{\partial p}a\right)$$

Using the identity: $$\frac{\partial}{\partial p}\det[M(p)] = \det[M(p)]tr\left[M(p)^{-1}\frac{\partial}{\partial p}M(p)\right]$$

We have $$\frac{\partial a}{\partial p} = \frac{\partial}{\partial p}\det[M(p)] = \det[M(p)]tr\left[M(p)^{-1}\frac{\partial}{\partial p}M(p)\right]$$

$$\frac{\partial b}{\partial p} = \frac{\partial}{\partial p}\det\left[M(p)^H\right] = \det\left[M(p)^H\right]tr\left[M(p)^{H^{-1}}\frac{\partial}{\partial p}M(p)^H\right]$$

Substitution yields:

$$\frac{\partial D}{\partial p} = \det\left[M(p)\right] tr\left[M(p)^{-1}\frac{\partial}{\partial p}M(p)\right]\det\left[M(p)^{H}\right] + \cdots$$

$$\det\left[M(p)^{H}\right] tr\left[M(p)^{H^{-1}}\frac{\partial}{\partial p}M(p)^{H}\right]\det\left[M(p)\right]$$

We want to reduce this so that it is in terms of the derivative of *K*; the reduced functions will vary according to system architecture. The following equations will be performed assuming the FSM architecture described in section 2.3.1. The following identities will be necessary to perform the reduction [4]:

$$\left(\det\left(M(p)\right)\right)^{H} = \det\left(M(p)^{H}\right)$$

$$(GK)^{H} = K^{H}G^{H}$$

$$\frac{\partial K^{H}}{\partial p} = \left(\frac{\partial K}{\partial p}\right)^{H} \text{ only if A matrix is symmetrical}$$

$$trace\left((GK)^{H}\right) = \left(trace(GK)\right)^{H}$$

$$trace(A+B) = trace(A) + trace(B)$$

$$trace(AB) = trace(BA)$$

$$A^{H^{-1}} = A^{-1^{H}} \text{ for A invertible}$$

Now we can start the reduction:

$$\frac{\partial D}{\partial p} = \left|\det\left[M(p)\right]\right|^2 \left(trace\left[M(p)^{-1} \frac{\partial}{\partial p}(GK) \right] + trace\left[M(p)^{H^{-1}} \frac{\partial}{\partial p}(GK)^H \right] \right)$$

Note the above equation may have a negative sign in front depending on system architecture.

$$\frac{\partial D}{\partial p} = \left|\det\left[M(p)\right]\right|^2 \left(trace\left[M(p)^{-1} G \frac{\partial K}{\partial p} \right] + trace\left[M(p)^{H^{-1}} \frac{\partial K^H}{\partial p} G^H \right] \right)$$

$$\text{Note}: \frac{\partial K^H}{\partial p} = \left(\frac{\partial K}{\partial p} \right)^H \text{, for } p = a_{ij} \text{ this holds only for } A_c \text{ symmetric}$$

$$\frac{\partial D}{\partial p} = \left|\det\left[M(p)\right]\right|^2 \left(trace\left[M(p)^{-1} G \frac{\partial K}{\partial p} \right] + trace\left[M(p)^{-1^H} \left(G \frac{\partial K}{\partial p} \right)^H \right] \right)$$

$$\frac{\partial D}{\partial p} = \left|\det\left[M(p)\right]\right|^2 \left(trace\left[M(p)^{-1} G \frac{\partial K}{\partial p} \right] + trace\left[\left(G \frac{\partial K}{\partial p} M(p)^{-1} \right)^H \right] \right)$$

$$\frac{\partial D}{\partial p} = \left|\det\left[M(p)\right]\right|^2 \left(trace\left[M(p)^{-1} G \frac{\partial K}{\partial p} \right] + trace\left[G \frac{\partial K}{\partial p} M(p)^{-1} \right]^H \right)$$

$$\frac{\partial D}{\partial p} = \left|\det\left[M(p)\right]\right|^2 \left(trace\left[M(p)^{-1} G \frac{\partial K}{\partial p} \right] + trace\left[M(p)^{-1} G \frac{\partial K}{\partial p} \right]^H \right)$$

If $\boldsymbol{trace}(\bullet) = \boldsymbol{a} + \boldsymbol{bj}$, then $\boldsymbol{trace}(\bullet)^{\boldsymbol{H}} = \boldsymbol{a} - \boldsymbol{bj}$
and $\boldsymbol{trace}(\bullet) + \boldsymbol{trace}(\bullet)^{\boldsymbol{H}} = (\boldsymbol{a} + \boldsymbol{bj}) + (\boldsymbol{a} - \boldsymbol{bj}) = 2(\mathrm{Re}(\boldsymbol{trace}(\bullet))) = 2\boldsymbol{a}$

$$\frac{\partial D}{\partial p} = 2\left|\det\left[M(p)\right]\right|^2 \mathrm{Re}\left(trace\left[M(p)^{-1} G \frac{\partial K}{\partial p} \right] \right)$$

Substituting back into $\frac{\partial}{\partial p}\frac{\sigma^2}{D} = \frac{-\sigma^2}{D^2}\frac{\partial D}{\partial p}$, where $D = \left|\det\left[M(p)\right]\right|^2 = ab$, yields

$$\frac{\partial}{\partial p}\frac{1}{d_{cr}^2(j\omega_k)} = \frac{\partial}{\partial p}\frac{\sigma^2}{D} = \frac{-2\sigma^2}{D}\mathrm{Re}\left(trace\left[M(p)^{-1}G\frac{\partial K}{\partial p}\right]\right)$$

Finally, substituting this back into $\frac{\partial \boldsymbol{S}_{cr}}{\partial \boldsymbol{p}_i} = \frac{1}{\pi}\sum_{k=1}^{n_\omega}\boldsymbol{W}_{cr}(\omega_k)\left[\frac{\partial}{\partial \boldsymbol{p}}\frac{1}{\boldsymbol{d}_{cr}^2(\boldsymbol{j}\omega_k)}\right]\Delta\omega_k$, yields

$$\frac{\partial S_{cr}}{\partial p_i} = \frac{-2}{\pi}\sum_{k=1}^{n_\omega}W_{cr}(\omega_k)\frac{1}{d_{cr}^2(j\omega_k)}\mathrm{Re}\left(trace\left[M(p)^{-1}G\frac{\partial K}{\partial p}\right]\right)\Delta\omega_k$$

Discrete State-Space *A* Matrix of the Actual FSM Compensator

0.5865	0.7726	0	0	0	0	0	0	0	0	0	0	0	0	0	0	0	0
-0.7726	0.5865	0	0	0	0	0	0	0	0	0	0	0	0	0	0	0	0
0	0	0.5961	0.7652	0	0	0	0	0	0	0	0	0	0	0	0	0	0
0	0	-0.7652	0.5961	0	0	0	0	0	0	0	0	0	0	0	0	0	0
0	0	0	0	0.6646	0.6988	0	0	0	0	0	0	0	0	0	0	0	0
0	0	0	0	-0.6988	0.6646	0	0	0	0	0	0	0	0	0	0	0	0
0	0	0	0	0	0	1.0000	0	0	0	0	0	0	0	0	0	0	0
0	0	0	0	0	0	0	0.6477	0.0026	0	0	0	0	0	0	0	0	0
0	0	0	0	0	0	0	-0.0026	0.6477	0	0	0	0	0	0	0	0	0
0	0	0	0	0	0	0	0	0	0.5865	0.7726	0	0	0	0	0	0	0
0	0	0	0	0	0	0	0	0	-0.7726	0.5865	0	0	0	0	0	0	0
0	0	0	0	0	0	0	0	0	0	0	0.5961	0.7652	0	0	0	0	0
0	0	0	0	0	0	0	0	0	0	0	-0.7652	0.5961	0	0	0	0	0
0	0	0	0	0	0	0	0	0	0	0	0	0	0.6646	0.6988	0	0	0
0	0	0	0	0	0	0	0	0	0	0	0	0	-0.6988	0.6646	0	0	0
0	0	0	0	0	0	0	0	0	0	0	0	0	0	0	1.0000	0	0
0	0	0	0	0	0	0	0	0	0	0	0	0	0	0	0	0.6477	0.0026
0	0	0	0	0	0	0	0	0	0	0	0	0	0	0	0	-0.0026	0.6477

Resources

All the code used to develop the results shown in section 4.3.1 can be obtained by contacting Haley Alexander via e-mail: haley.e.alexander@boeing.com or UltraViolet002@hotmail.com.

REFERENCES

[1] G. J. Mallory, D. W. Miller, *Development and Experimental Validation of Direct Controller Tuning for Spaceborne Telescopes*, Ph.D. thesis, Massachusetts Institute of Technology, April 2000, SERC Report #1-2000

[2] T. S. VanZwieten, G. M. Bower, S. L. Lacy, "Data-Based Control of a Free-Free Beam in the Presence of Uncertainty", *American Control Conference*, pp. 31-36, 2007.

[3] S. Lacy, K. Schrader, R. Fuentes, V. Babuska, J. Goodding, "The Deployable Optical Telescope", *Final Report AFRL-VS-TR-2005-XXXX*, 2005.

[4] J.M. Maciejowski, *Multivariable Feedback Design*, Addison-Wesley Publishing Company, 1989.

[5] D.S. Bernstein, *Matrix Mathematics: Theory, Facts, and Formulas with Application to Linear Systems Theory*, Princeton University Press, 2005.

[6] Peter Dorato, Chaouki T. Abdallah, Vito Cerone, *Linear Quadratic Control: An Introduction*, Krieger Publishing Company, 2000.

[7] Gene F. Franklin, J. David Powell, Abbas Emami-Naeini, *Feedback Control of Dynamic Systems: Fourth Edition*, Prentice-Hall, Inc., 2002.

[8] Sigurd Skogestad, Ian Postlethwaite, *Multivariable Feedback Control, Analysis and Design: Second Edition*, John Wiley & Sons Ltd, 2005.

[9] P.K. Stevens, "A Generalization of the Nyquist Stability Criterion," *IEEE Transactions on Automatic Control*, vol. 26, no. 3, pp. 664-669, 1981.

[10] Charles A. Desoer, Yung-Terng Wang, "On the Generalized Nyquist Stability Criterion," *IEEE Transactions on Automatic Control,* vol. ac-25, no. 2, 1980.

[11] Steven A. Lane, Seth L. Lacy, Vit Babuska, Stephen Hanes, Karl Schrader, Robert Fuentes, "Active Vibration Control of a Deployable Optical Telescope," *Journal of Spacecraft and Rockets*, vol. 45, no. 3, pp. 568-586, 2008.

[12] M. J. Balas, "Trends in Large Space Structure Control Theory: Fondest Hopes, Wildest Dreams," *IEEE Transactions on Automatic Control*, vol. 27, no. 3, pp. 522-535, June 1982.

[13] S. L. Lacy, V. Babuska, K. N. Schrader, and R. Fuentes, "System Identification of Space Structures," *American Control Conference*, Portland, OR, June 2005.

[14] D. W. Sparks, J. Juang, "Survey of Experiments and Experimental Facilities for control of Flexible Structures", *Journal of Guidance, Control, and Dynamics*, Vol. 15, No. 4, pp. 801-816, 1992.

[15] A. Carrier, J. Aubrun, "Modal Characterization of the ASCIE Segmented Optics Testbed: New Algorithms and Experimental Results," *Controls for Optical Systems*, edited by J. A. Breakwell, Proceedings of SPIE – The International Society for Optical Engineering, Vol. 1696, Society of Photo-Optical Instrumentation Engineers (International Society for Optical Engineering), Bellingham, WA, pp. 193-208, 1992.

[16] D. S. Acton, P. D. Atcheson, M. Cermak, L. K. Kinsbury, "James Webb Space Telescope Wave-Front Sensing and Control Algorithms," *Optical, Infrared and Millimeter Space Telescopes*, edited by J. C. Mather, Proceedings of SPIE – The International Society for Optical Engineering, Vol. 5487, Society of Photo-Optical Instrumentation Engineers (International Society for Optical Engineering), Bellingham, WA, pp. 887-896, 2004.

[17] E. A. Valazquez, A. Pujari, H. H. Bossalis, K. Rad, "Frequency Domain System Identification of Large Segmented Space Reflector," *2005 IEEE International Symposium on Intelligent Control*, Vol. 1, Inst. Of Electrical and Electronics Engineers, Piscataway, NJ, pp.497-500, 2005.

[18] J. Z. Lou, D. Redding, N. Sigrist, Y. Zhang, S. Basinger, "JWST On-Orbit Multi-Field Wave-Front Control with a Kalman Filter," *Optical Modeling and Performance Predictions II*, edited by M. A. Kahan, Proceedings of SPIE – The International Society for Optical Engineering, Vol. 5867, Society of Photo-Optical Instrumentation Engineers (International Society for Optical Engineering), Bellingham, WA, pp. 58670T-1-58670T-14, 2005.

[19] M. W. Fitzmaurice, K. Q. Ha, C. Le, J. M. Howard, "End-to-End Performance Modeling of the James Webb Space Telescope (JWST) Observatory," *Optical Modeling and Performance Predictions II*, Proceedings of SPIE – The International Society for Optical Engineering, Vol. 5867, edited by M. A. Kahan, Society of Photo-Optical instrumentation Engineers (International Society for Optical Engineering), Bellingham, WA, pp. 58670W-1-58670W-14, 2005.

[20] L. M. R. Hardaway, L. D. Peterson, "Nanometer Scale Spontaneous Vibrations in a Deployable Truss Under Mechanical Loading," *AIAA Journal*, Vol. 40, No. 10, pp. 2070-2076, Oct. 2002.

[21] K. D. Bell, M. K. Powers, S. F. Griffin, S. M. Huybrechts, "Air Force Research Laboratory's Technology Programs Addressing Deployable Space Optical Systems," *Space Telescopes and INstrumnets V*, edited by P. Y. Bely and J. B. Breckinridge, Proceedings of SPIE – The International Society for Optical Engineering, Vol. 3356, Society of Photo-Optical Instrumentation Engineers (International Society for Optical Engineering), Bellingham, WA, pp. 535-551, 1998.

[22] L. Robertson, S. F. Griffin, M. K. Powers, R. Cobb, "Current Status of the UltraLITE Control Technology Testbed for Optical Mirror Mass Control," *Novel Optical Systems and Large Aperture Imaging Systems*, edited by K. D. Bell, M. K. Powers, and J. M. Sasian, Proceedings of SPIE-The International Society for Optical Engineering, Vol. 3430, Society of Photo-Optical Instrumentation Engineers (International Society for Optical Engineering), Bellingham, WA, pp. 209-218, 1998.

[23] S. F. Griffin, L. Robertson, S. M. Huybrechts, "Ultra-Lightweight Structures for Deployable Optics, " *Novel Optical Systems and Large Aperture Imaging Systems*, edited by K. D. Bell, M. K. Powers, and J. M. Sasian, Proceedings of SPIE-The International Society for Optical Engineering, Vol. 3430, Society of Photo-Optical Instrumentation Engineers (International Society for Optical Engineering), Bellingham, WA, pp. 219-226, 1998.

[24] K. Denoyer, R. Erwin, R. Ninneman, "Advanced Smart Structures Flight Experiments for Precision Spacecraft," *Acta AstronauticaI*, Vol. 47, No. 2-9, pp. 389-397, 2000.

[25] V. Babuska, R. Erwin, L. Sullivan, "System Identification of the SUITE Isolation Platform: Comparison of Ground and Flight Experiments," *AIAA Structures, Structural Dynamics, and Materials Conference – Smart Damping and Isolation*, Vol. 3, AIAA, Reston, VA, pp. 2185-2195, 2003.

[26] C. Blaurock, *Dynamod Users Manual*, Midé Technology Corporation, 200 Boston Ave, Suite 1000, Medford, MA 02155, 2003.

[27] PAM-VA One, Software Package, Ver. 1.1, ESI Group, Paris, 2005.

[28] R. N. Jacques, K. Liu, D. W. Miller, "Identification of Highly Accurate Low Order State Space Models in the Frequency Domain," *Signal Processing*, Vol. 52, No. 2, pp. 195-207, July 1996.

[29] K. Liu, R. N. Jacques D. W. Miller, "Frequency Domain Structural System Identification by Observability Range Space Extraction," *Journal of Dynamics Systems Measurement and Control*, Vol. 118, pp. 211-220, 1996.

[30] T. McKelvey, H. Akcay, L. Ljung, "Subspace-based Identification of Infinite-dimensional Multivariable Systems from Frequency-response Data," *Automatica*, Vol. 32, No. 6, pp. 885-902, June 1996.

[31] R. Pintelon, J. Schoukens, *System Identification: A Frequency Domain Approach*, Piscataway, NJ: IEEE Press, 2001.

[32] S. Lane, L. Lacy, V. Babuska, D. Carter, "Correlation and Error Metric for Plant Identification of On-Orbit Space Structures," *Journal of Spacecraft and Rockets*, Vol. 44. No. 3, pp. 710-721, May-June 2007.

[33] S. Lacy, V. Babuska, "Input-Output Data Scaling for System Identification," *Proceedings of the International Federations of Automatic Control Symposium on System Identification* [CD-ROM], Elsevier, Oxford, 2006.

[34] M. S. Lake, L. D. Peterson, M. B. Levine, "Rationale for Defining Structural Requirements for Large Space Telescopes," *Journal of Spacecraft and Rockets*, Vol. 39, No. 5, pp. 674-681, 2002.

[35] F. Bourgault, *Model Uncertainty and Performance Analysis for Precision controlled Space Structures*, Master's thesis, Massachusetts Institute of Technology, Space Systems Laboratory, May 2000.

[36] H. L. Gutierrez, *Performance Assessment and Enhancement of Precision Controlled Structures During Conceptual Design*, Ph.D. thesis, Massachusetts Institute of Technology, February 1999, SERC Report #1-99.

[37] E. H. Anderson, *Robust Placement of Actuators and Dampers for Structural Control*, Ph.D. thesis, Massachusetts Institute of Technology, SERC Report #14-93, October 1993.

[38] M. Mercadal, "Homotopy Approach to Optimal, Linear Quadratic Fixed Architecture Compensation," *Journal of Guidance, Control, and Dynamics,* Vol. 14, No. 6, pp. 1224-1233, 1991.

[39] A. Hassibi, J. P. How, S. P. Boyd, "Low-Authority Controller Design by Means of Convex Optimization," *Journal of Guidance and Control*, Vol. 22, No. 6, pp. 862-872, 1999.

[40] G. J. Mallory, D. W. Miller, "Decentralized State Estimation for Flexible Space Structures," *Journal of Guidance, Control, and Dynamics*, Vol. 23, No. 4, pp. 665-672, 2000.

[41] W. Gawronsk, K. B. Lim, "Balanced Actuator and Sensor Placement for Flexible Structures," *International Journal of Control*, Vol. 65, No.1, pp. 131-125, 1996.

[42] K. B. Lim, "Method for Optimal Actuator and Sensor Placement for Large Flexible Structures," *Journal of Guidance and Control*, Vol. 15, No. 1, pp. 49-57, 1992.

[43] W. N. McCasland, *Sensor and Actuator Selection for Fault-Tolerant Control of Flexible Structures*, Ph.D. thesis, Massachusetts Institute of Technology, February 1989.

[44] P. G. Maghami, S. M. Joshi, "Sensor-Actuator Placement for Flexible Structures with Actuator Dynamics," *Journal of Guidance and Control*, Vol. 16, No. 2, pp. 301-307, 1993.

[45] R. E. Skelton, P. C. Hughes, "Modal Cost Analysis for Linear Matrix-Second-Order Systems," *Journal of Dynamics, Measurement and Control*, Vol. 102, pp. 151-158, 1980.

[46] R. E. Skelton, D. Chiu, "Optimal Selection of Inputs and Outputs in Linear Stochastic Systems", *Journal of Astronautical Sciences*, Vol. XXXI, pp. 399-414, 1983.

[47] C. Y. Lin, *Towards Optimal Strain Actuated Aeroelastic Control*, Ph.D. thesis, Massachusetts Institute of Technology, February 1996.

[48] R. E. Skelton, M. L. DeLorenzo, "Selection of NoisyActuators and Sensors in Linear Stochastic Systems," *Large Scale Systems Theory and Applications*, Vol. 4, pp. 109-136, 1983.

[49] Y. Kim, J. L. Junkins, "Measure of Controllability for Actuator Placement," *Journal of Guidance and Control*, Vol. 14, No. 5, pp. 895-902, 1991.

[50] H. Kwakernaak, R. Sivan, *Linear Optimal Control Systems*, John Wiley & Sons, Inc., 1972.

[51] K. Zhou, J. C. Doyle, K. Glover, *Robust and Optimal Control*, Prentice Hall Inc., 1996.

[52] S. C. O. Grocott, *Comparison of Control Techniques for Robust Performance on Uncertain Sructural Systems*, S.M. thesis, Massachusetts Institute of Technology, SERC Report #2-94, January 1994.

[53] N. K. Gupta, "Frequency-Shaped Cost Functionals: Extension of Linear-Quadratic-Gaussian Design Methods," *Journal of Guidance and Control*, Vol. 3, No. 6, pp. 529-535, 1980.

[54] Lublin L., S. Grocott, M. Athans, "H_2 and H_∞ Control," In *The Control Handbook,* CRC Press, 1996.

[55] K. Okada, R. E. Skelton, "Sensitivity Controller for Uncertain Systems," *Journal of Guidance, Control, and Dynamics*, Vol. 13, No. 2, pp. 321-329, 1990.

[56] B. Masters, *Evolutionary Design of Controlled Structures*, Ph.D. thesis, Massachusetts Institute of Technology, April 1997. SERC Report #1-97.

[57] D. C. Youla, H. A. Jabr, J. J. Bongiorno, "Modern Wiener-Hopf design of optimal controllers: part II," *IEEE Transactions on Automatic Control*, Vol. AC-21, No. 3, pp. 319-338, June 1976.

[58] S. P. Boyd, V. Balakrishnan, C. H. Barratt, N. M. Khraishi, X. Li, D. G. Meyer, S. T. Norman, "A New CAD Method and Associated Architectures for Linear Controllers," *IEEE Transactions on Automatic Control,* Vol. 33, No. 3, pp. 268-283, 1988.

[59] E. Polak, S. E. Salcudean, "On the Design of Linear Multivariable Feedback Systems Via Constrained Nondifferentiable Optimization in H^{∞} Spaces," *IEEE Transactions on Automatic Control,* Vol. 34, No. 3, pp. 268-276, 1989.

[60] S. P . Boyd, C. H. Barratt, *Linear Control Design, Limits of Performance*, New Jersey: Prentice-Hall Inc., 1991.

[61] L. K. McGovern, *A Constrained Optimization Approach to Control with Application to Flexible Structures*, Ph.D. thesis, Massachusetts Institute of Technology, May 1996.

[62] B. V. Lintereur, *Constrained Design via Convex Optimization with Application*, S.M. thesis, Massachusetts Institute of Technology, May 1998.

[63] D. C. Hyland, D. S. Bernstein, "The Optimal Projection Equations for Fixed-Order Dynamic Compensation," *IEEE Transactions on Automatic Control,* Vol. 29, No. 11, pp. 1034-1037, 1984.

[64] E. G. Collins, D. Sadhukhan, "A Comparison of Descent and Continuation Algorithms for H_2 Optimal, Reduced-Order Control Designs," *International Journal of Control*, Vol. 69, No. 5, pp 647-663, 1998.

[65] U.-L. Ly, A. E. Bryson, R. H. Cannon, "Design of Low-order Compensators using Parameter Optimization," *Automatica*, Vol. 21, No. 3, pp. 315-318, 1985.

[66] U.-L. Ly, *Multivariable Control System Design Using Nonlinear Programming*, Department of Aeronautics and Astronautics Report, University of Washington, Seattle WA, 1998.

[67] D. G. MacMartin, S. R. Hall, D. S. Bernstein, "Fixed Order Multi-Model Estimation and Control," *Proceedings of the American Control Conference*, Boston, MA, June 1991.